Check for updates

The High Energy X-ray Probe (HEX-P): supernova remnants, pulsar wind nebulae, and nuclear astrophysics

Stephen Reynolds[1], Hongjun An[2], Moaz Abdelmaguid[3], Jason Alford[3], Chris Fryer[4], Kaya Mori[5]*, Melania Nynka[6], Jaegeun Park[2], Yukikatsu Terada[7,8], Jooyun Woo[5], Aya Bamba[9,10,11], Priyadarshini Bangale[12], Rebecca Diesing[13], Jordan Eagle[14], Stefano Gabici[15], Joseph Gelfand[3], Brian Grefenstette[16], Javier Garcia[14], Chanho Kim[2], Sajan Kumar[17], Brydyn Mac Intyre[18], Kristin Madsen[14], Silvia Manconi[19], Yugo Motogami[7], Hayato Ohsumi[7], Barbara Olmi[20,21], Toshiki Sato[22], Ruo-Yu Shang[23], Daniel Stern[24], Naomi Tsuji[25], George Younes[14] and Andreas Zoglauer[26]

[1]Department of Physics, North Carolina State University, Raleigh, NC, United States, [2]Department of Astronomy and Space Science, Chungbuk National University, Cheongju, Republic of Korea, [3]Department of Physics, New York University, Abu Dhabi, United Arab Emirates, [4]Center for Non Linear Studies, Los Alamos National Laboratory, Los Alamos, NM, United States, [5]Columbia Astrophysics Laboratory, Columbia University, New York, NY, United States, [6]Kavli Institute for Astrophysics and Space Research, Massachusetts Institute of Technology, Cambridge, MA, United States, [7]Graduate School of Science and Engineering, Saitama University, Sakura, Saitama, Japan, [8]Japan Aerospace Exploration Agency (JAXA), Institute of Space and Astronautical Science, Sagamihara, Japan, [9]Department of Physics, The University of Tokyo, Tokyo, Japan, [10]Research Center for the Early Universe, School of Science, The University of Tokyo, Tokyo, Japan, [11]Trans-Scale Quantum Science Institute, The University of Tokyo, Tokyo, Japan, [12]Department of Physics and Astronomy, Bartol Research Institute, University of Delaware, Newark, DE, United States, [13]Department of Astronomy and Astrophysics, The University of Chicago, Chicago, IL, United States, [14]NASA Goddard Space Flight Center, Greenbelt, MD, United States, [15]Universite Paris Cite, Centre National de la Recherche Scientifique, Astroparticule et Cosmologie, Paris, France, [16]Space Radiation Laboratory, California Institute of Technology, Pasadena, CA, United States, [17]Department of Physics, University of Maryland, College Park, MD, United States, [18]Department of Physics and Astronomy, University of Manitoba, Winnipeg, MB, Canada, [19]Laboratoire d'Annecy-le-Vieux de Physique Theorique, Centre National de la Recherche Scientifique, Université Savoie Mont Blanc, Annecy, France, [20]INAF—Osservatorio Astrofisico di Arcetri, Firenze, Italy, [21]INAF—Osservatorio Astronomico di Palermo, Palermo, Italy, [22]Department of Physics, School of Science and Technology, Meiji University, Kanagawa, Japan, [23]Department of Physics and Astronomy, Barnard College, New York, NY, United States, [24]Jet Propulsion Laboratory, California Institute of Technology, Pasadena, CA, United States, [25]Faculty of Science, Kanagawa University, Kanagawa, Japan, [26]Space Sciences Laboratory, University of California, Berkeley, Brkeley, CA, United States

HEX-P is a probe-class mission concept that will combine high spatial resolution X-ray imaging (<10″ full width at half maximum) and broad spectral coverage (0.2−80 keV) with an effective area far superior to current facilities (including *XMM*-Newton and *NuSTAR*) to enable revolutionary new insights into a variety of important astrophysical problems. HEX-P is ideally suited to address important problems in the physics and astrophysics of supernova remnants (SNRs) and pulsar wind nebulae (PWNe). For shell SNRs, HEX-P can greatly improve our understanding via more accurate spectral characterization and localization of non-thermal X-ray emission from both

non-thermal-dominated SNRs and those containing both thermal and non-thermal components, and can discover previously unknown non-thermal components in SNRs. Multi-epoch HEX-P observations of several young SNRs (e.g., Cas A and Tycho) are expected to detect year-scale variabilities of X-ray filaments and knots, thus enabling us to determine fundamental parameters related to diffusive shock acceleration, such as local magnetic field strengths and maximum electron energies. For PWNe, HEX-P will provide spatially-resolved, broadband X-ray spectral data separately from their pulsar emission, allowing us to study how particle acceleration, cooling, and propagation operate in different evolution stages of PWNe. HEX-P is also poised to make unique and significant contributions to nuclear astrophysics of Galactic radioactive sources by improving detections of, or limits on, ^{44}Ti in the youngest SNRs and by potentially discovering rare nuclear lines as evidence of double neutron star mergers. Throughout the paper, we present simulations of each class of objects, demonstrating the power of both the imaging and spectral capabilities of HEX-P to advance our knowledge of SNRs, PWNe, and nuclear astrophysics.

1 Introduction

In the Galactic ecosystem, fast particles play a crucial role in ionization of molecular material (influencing star and planet formation), in regulating the interstellar magnetic field, and perhaps in driving a Galactic wind. We observe a highly filtered subset of those particles as cosmic rays at Earth, but their origins lie in a range of high-energy-density Galactic environments. Strong shock waves from supernova remnants (SNRs) remain the prime candidate for accelerating the bulk of Galactic cosmic-ray electrons and ions up to energies of the order of PeV, through the diffusive shock acceleration (DSA) mechanism. An additional leptonic component (electrons and positrons) is thought to originate in pulsar wind nebulae (PWNe), probably at the termination shock of the initially relativistic cold outflow. These classes of object exhibit the physics of particle acceleration in particularly accessible ways, through spatially resolved nonthermal emission in radio, X-ray, and gamma-ray bands. That emission is due to some combination of four important processes, three involving leptons and one due to hadrons. The leptonic processes, described in more detail in Mori et al. (2021), are synchrotron radiation producing radio through hard X-ray emission, inverse-Compton upscattering of ambient photon fields producing GeV to TeV gamma rays, and nonthermal bremsstrahlung producing hard X-rays through gamma rays. Of these, the latter is rarely dominant. The hadronic process begins with inelastic collisions of energetic ions with ambient thermal gas, producing charged and neutral pions (once the kinematic threshold of about 140 MeV is surpassed). The charged pions decay, ultimately, to secondary electrons and positrons which can produce synchrotron radiation, in an inescapable consequence of the hadronic process. The neutral pions decay to gamma rays, which can range in energy up to ten percent or so of that of the initiating hadron. One of the fundamental questions in interpreting potential Galactic cosmic-ray sources involves deciding which process is responsible for their gamma-ray emission.

This paper demonstrates the potential contributions to understanding these issues that can be provided by a high resolution, high sensitivity hard X-ray imaging capability. In addition to access to the continuum processes described above, the hard X-ray spectral region offers a window into some of the most energetic stellar-scale processes in Nature: along with supernovae and SNRs, the kilonovae resulting from merging binary neutron stars. In both these arenas, nucleosynthesis is important and can be diagnosed through the production of unstable species with a range of half-lives which decay with the production of different hard X-ray lines. Of particular relevance for SNe and young SNRs are the 68 and 78 keV lines produced in the decay of ^{44}Ti, but merging neutron stars are also expected to produce potentially observable lines for a sufficiently nearby event. Information from such decays gives insight into nucleosynthesis unavailable in any other channel.

The HEX-P instrument can bring to the study of these issues unmatched sensitivity and angular resolution above 10 keV. Below, we lay out the contributions HEX-P can make to characterizing the nature and evolution of SNRs and PWNe. §2 describes the current telescope design and HEX-P simulation tools. §3 demonstrates HEX-P's spectro-imaging capabilities for characterizing thermal and non-thermal X-ray emission from young SNRs by showing simulation results for Cas A, Tycho, G1.9 + 0.3, and SN 1987A. §4 presents HEX-P's observation program of investigating different evolutionary stages of PWNe and exploring this primary class of leptonic particle accelerators in our Galaxy. HEX-P's broad-band X-ray data, in conjunction with the upcoming Cherenkov Telescope Array (CTA) mission, will allow us to dissect the particle acceleration, propagation, and cooling processes in PWNe. §5 discusses HEX-P's unique role in nuclear astrophysics, such as detecting ^{44}Ti lines from the youngest SNRs and nuclear lines from double neutron star mergers in our Galaxy. In our

companion paper (Mori et al., submitted to FrASS), we will discuss other types of Galactic particle accelerators such as unidentified PeVatron candidates, star clusters, superbubbles, microquasar jets, TeV gamma-ray binaries and the supermassive black hole in Sgr A*. The science we describe here has considerable overlap with that discussed in parallel HEX-P papers. Our planned studies of PWNe will of course also produce important new information on the pulsars they contain (see Jaodand et al., submitted to FrASS), with possible bearing on magnetars (Alford et al., submitted to FrASS) and general properties of neutron stars (Ludlum et al., submitted to FrASS) as well. Various classes of binary X-ray source are also described in Connors et al. (submitted to FrASS). Several of our target sources may be observed as part of the Galactic Center effort (Mori et al., submitted to FrAss), while others lie in nearby galaxies (Lehmer et al., submitted to FrASS). SN 1987A is on our list of primary targets, and we describe here some of the nuclear astrophysics possible with SNe or neutron-star mergers, more likely to be found among nearby galaxies than in our own.

2 HEX-P mission design and simulation

The High-Energy X-ray Probe (Madsen et al., 2023) is a probe-class mission concept that offers sensitive broad-band coverage (0.2–80 keV) of the X-ray spectrum with exceptional spectral, timing, and angular capabilities. It features two high-energy telescopes (HET) that focus hard X-rays, and a low-energy telescope (LET) providing soft X-ray coverage.

The LET consists of a segmented mirror assembly coated with Ir on monocrystalline silicon that achieves a half power diameter of $3.5''$, and a low-energy DEPFET detector, of the same type as the Wide Field Imager (WFI; Meidinger et al., 2020) onboard Athena (Nandra et al., 2013). It has 512×512 pixels that cover a field of view of $11.3' \times 11.3'$. It has an effective bandpass of 0.2–25 keV and a full-frame readout time of 2 ms, and can be operated in 128 and 64 channel window modes for higher count-rates to mitigate pile-up and allow faster readout. Pile-up effects remain below an acceptable limit of ~1% for sources up to ~100 mCrab in the smallest window configuration (64w). Excising the core of the point-spread function (PSF), a common practice in X-ray astronomy, will allow for observations of brighter sources, with a maximum loss of ~60% of the total photon counts.

The HET consists of two co-aligned telescopes and detector modules. The optics are made of Ni-electroformed full shell mirror substrates, leveraging the heritage of *XMM* (Jansen et al., 2001), and coated with Pt/C and W/Si multilayers for an effective bandpass of 2–80 keV. The high-energy detectors are of the same type as those flown on *NuSTAR* (Harrison et al., 2013), and they consist of 16 CZT sensors per focal plane, tiled 4×4, for a total of 128×128 pixels spanning a field of view slightly larger than for the LET, of $13.4' \times 13.4'$.

All the simulations presented here were produced with a set of response files that represent the observatory performance based on current best estimates (Madsen et al., 2023). The effective area is derived from a ray-trace of the mirror design including obscuration by all known structures. The detector responses are based on simulations performed by the respective hardware groups, with an

optical blocking filter for the LET and a Be window and thermal insulation for the HET. The LET background was derived from a GEANT4 simulation (Eraerds et al., 2021) of the WFI instrument, and the one for the HET from a GEANT4 simulation of the *NuSTAR* instrument, both positioned at L1. Throughout the paper, we present our simulation results for *HEX-P* using the SIXTE (Dauser et al., 2019) and XSPEC toolkits (Arnaud, 1996). To ensure the most realistic simulation results, we incorporated recent high-resolution X-ray images (mostly from *Chandra* or other wavelength observations), the best-known spectral information, and theoretical model predictions. Various exposure times have been considered for the feasibility studies presented in the following sections.

3 Supernova remnants

The best understood of all sources of high-energy particles are probably the shell SNRs, where independent measures of the ambient densities, shock speeds, and magnetic-field strengths are all possible. However, the evidence for those high-energy particles is primarily synchrotron X-ray emission, unambiguously separable from thermal emission only at energies above 10 keV or so. *NuSTAR* showed the promise of studying particle acceleration in SNRs with a few observations of young bright SNRs with strong nonthermal emission relative to thermal, but those observations raised more questions than they answered. HEX-P will be able to identify and characterize hard nonthermal X-ray emission in many more remnants, and will be able to address many of the questions raised by earlier observations. Older SNRs with somewhat slower shock velocities, predicted by theory to accelerate electrons to X-ray-emitting energies but too faint for prior study, can be examined by HEX-P, along with potential new sources turned up by upcoming surveys such as that performed by eROSITA, and newly occurring transients that may appear. Below we illustrate the capabilities of HEX-P with simulations of Cas A, Tycho, G1.9 + 0.3 (youngest Galactic SNR), and SN 1987A.

3.1 Thermal emission

Supernova remnants in X-rays are chiefly thermal sources, with temperatures from a few tenths to a few keV, and rich line spectra providing essential information on plasma composition, and given sufficient energy resolution, on radial velocities and ionization state. See Vink (2012) for a review. Most young remnants (estimated ages less than a few thousand years) also show spatial and spectral evidence for nonthermal X-rays, often in the form of thin rims at the remnant periphery, and in hard continuum components sometimes apparent in relatively line-free regions of the spectrum between 4 and 6 keV. Some of the continuum emission in this spectral region is certainly thermal bremsstrahlung, and interpreting the Fe Kα line complex at 6.4–6.7 keV requires knowing the thermal fraction. The nonthermal component can be followed to higher energies. Non-imaging instruments before *Chandra* and *XMM* found hard continua in the integrated spectra of a few remnants, the most spectacular being Cas A, with emission extending to at least 100 keV (Vink et al., 2000). But few remnants are bright enough to be studied in this way. *NuSTAR* was able to detect non-thermal continua in a

few young remnants, to 20 keV or (in a few cases) 30 keV. But in others, where small features in Chandra images are found to be line-free, the integrated emission at energies above 10 keV is not strong enough to be examined with *NuSTAR*.

The ability to identify thermal and nonthermal emission components in SNRs below about 10 keV would provide a powerful tool for diagnosing the detailed relation between particle acceleration and the properties of the thermal plasma. HEX-P's two instruments will provide such a tool. One simple but critical distinction would be to differentiate shocked ejecta from shocked surrounding material (undisturbed interstellar medium [ISM], for remnants of SNe Ia, or modified stellar wind or circumstellar material for remnants of core-collapse SNe), requiring good spatial and spectral resolution in the line-rich region from 0.5 to 4 keV, as well as at the crucial Fe Kα line. While it is possible to piece together some of this information by combining *Chandra* or *XMM* observations with, say, *NuSTAR* data, the task is complex in practice. Having two instruments aboard the same spacecraft will significantly improve our ability to cross-calibrate and will result in unbroken spectra from as low energies as interstellar absorption typically permits ($\gtrsim 0.2$ keV) up to 80 keV if such photons are present. SNR plasmas are generally multitemperature, and while they can sometimes be fairly well represented by two components, a higher-temperature component is easy to confuse with nonthermal emission, with important effects on interpreting, say, the equivalent width of the Fe Kα line complex. In fact, the LET instrument alone, coupled with HEX-P's large effective area, will improve the purely thermal diagnosis of many SNRs. Particle backgrounds constitute significant impediments above 8 or 9 keV for both *Chandra* and *XMM*, but can be expected to be significantly lower at the L1 position of HEX-P.

3.2 Nonthermal continuum

The presence in most young SNRs of strong thermal X-ray emission is both a bug and a feature: below 10 keV, the fraction of nonthermal emission is often quite uncertain, but as described above, thermal emission provides essential information on densities and shock speeds, and composition. Observing those objects at X-ray energies above 10 keV where the thermal contribution is small or negligible then allows the separate characterization of the nonthermal-electron energy spectrum. Basic questions afflict our understanding of electron acceleration to high energies in young SNRs. Where, exactly, does the acceleration take place? What are the physical conditions there, as indicated by observations at other wavelengths? What are the spectral shapes? To how high photon energies does emission extend, and are there spatial variations in spectral shape? The current fleet of X-ray observatories has produced important information on some of these questions, but the acceleration to the highest energies remains mysterious. Only *NuSTAR* has been able to image SNRs well above thermal energies, and spatial resolution, effective area, and background limitations have confined those studies to a few objects. But what has been learned is alarming: especially in Cas A, both spectral and spatial expectations for the highest-energy synchrotron emission were impressively upended. Neither the forward nor the reverse shock seems to be the site of the strongest emission between 15 and 50 keV.

The spectra, while steeper than radio, show no indication of further curvature, indicating that the highest-energy electrons have not yet been observed. Observations of the handful of other young SNRs bright enough above 10 keV for *NuSTAR* hint at similar deficiencies.
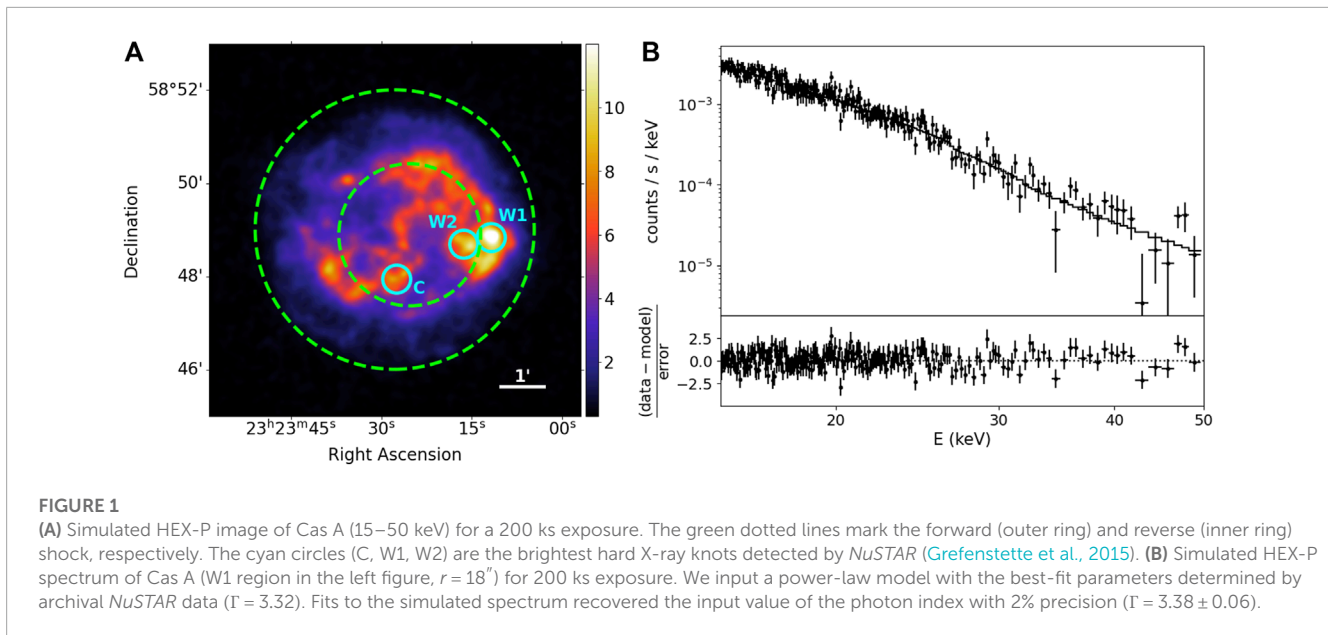
But this problem is an opportunity. The study of particle acceleration in shocks has seemed to be an essentially solved problem, with the only remaining tasks to measure the parameters of the standard models. But those standard models are clearly incomplete, in the face of the *NuSTAR* data. More detailed observations above 10 keV of not only the historical remnants but other young objects less well-known, stand to produce qualitatively new information most relevant to basic questions of efficiency and maximum energies attainable (e.g., Diesing and Caprioli (2021)) that may apply to acceleration sites elsewhere in the Universe.

3.3 Cassiopeia A

Cassiopeia A (Cas A) is the youngest remnant of a core-collapse supernova event in our Galaxy. Light-echo observations of the scattered optical emission from the supernova event (Krause et al., 2008a) have established the supernova subtype as IIb—the explosion of a massive star that lost most of its hydrogen envelope, and has expanded into the pre-SN stellar wind. Its radio emission is dramatically stronger than that from any other Galactic SNR, perhaps partly due to the blast wave having encountered dense stellar wind at earlier times. The strongest radio emission from electrons with GeV energies is found not at the outer blast wave but at a bright inner ring between the forward and reverse shocks, where strong magnetic turbulence is likely to be present, boosting synchrotron emissivity because of a stronger magnetic field but also perhaps further accelerating nonthermal particles. These properties distinguish Cas A from young remnants of Type Ia supernovae such as Tycho and Kepler, which expand into inhomogeneous, but probably not radially varying, interstellar medium, and whose radio emission tends to be concentrated at the forward shock.

While the bright radio ring in Cas A indicates a large population of GeV-energy electrons, it was expected that the highest-energy X-ray-emitting particles would be found at the primary acceleration sites in the remnant, probably the forward blast wave. Evidence for particle acceleration at reverse shocks in young SNRs is ambiguous at best. The *NuSTAR* observations (Grefenstette et al., 2015), however, told a different story, showing diffuse hard X-ray (> 15 keV) emission from the remnant interior, with the brightest emission from two compact knots inside the blast wave to the west. Hard emission is present and associated with the outer blast wave, but it is considerably fainter. There are approximate correspondences between the bright knots and features in radio or soft X-rays (Bleeker et al., 2001; Helder and Vink, 2008; Maeda et al., 2009), where they are much less prominent. The angular resolution and sensitivity of *NuSTAR* were insufficient to allow a detailed search for corresponding small-scale features at optical wavelengths, where proper motions and/or radial velocities might give clues as to the nature of these hotspots of electron acceleration.

HEX-P, with improved angular resolution and sensitivity, will allow for resolving faint features such as shown in Figure 1. Non-thermal spectra will be mapped at the forward shock, reverse shock, and interior of the remnant. This spatially resolved

FIGURE 1
(A) Simulated HEX-P image of Cas A (15−50 keV) for a 200 ks exposure. The green dotted lines mark the forward (outer ring) and reverse (inner ring) shock, respectively. The cyan circles (C, W1, W2) are the brightest hard X-ray knots detected by *NuSTAR* (Grefenstette et al., 2015). **(B)** Simulated HEX-P spectrum of Cas A (W1 region in the left figure, $r = 18''$) for 200 ks exposure. We input a power-law model with the best-fit parameters determined by archival *NuSTAR* data ($\Gamma = 3.32$). Fits to the simulated spectrum recovered the input value of the photon index with 2% precision ($\Gamma = 3.38 \pm 0.06$).

spectroscopy will provide the best opportunity to study the variability on timescales of a few years of non-thermal emission at the hard X-ray knots suggested by Sato et al. (2018) and Uchiyama and Aharonian (2008). Such flux variability requires enhanced magnetic fields (0.1–1 mG) perhaps at "inward shocks" induced by a density gradient due to molecular clouds (Fraschetti et al., 2018) or asymmetric circumstellar material (Orlando et al. (2022) and references therein). While Sato et al. (2018) left open the possibility of variable thermal emission ($kT \sim 1$–3 keV) from *Chandra* observations, the high-energy sensitivity of HEX-P HET will minimize the complication with thermal emission and probe clean non-thermal continuum with photon index $\Gamma = 3$–3.5 above 15 keV as seen by *NuSTAR*. Independent estimates of the magnetic field (such as those based on "thin rim" morphology; Parizot et al., 2006) are also of order 0.2 mG, giving synchrotron cooling timescales of 1–10 years. Our simulation shows that a 200-ks observation with HEX-P can measure the flux of the hard X-ray knots ($r = 18''$ circles) at 2% precision. At this level of angular resolution and precision of flux measurement, the magnetic field can be accurately measured not only at the inward shock but also at other smaller hard X-ray knots throughout the entire remnant. Such a study will reveal the magnetic field structure of the remnant at the location of the highest-energy electrons, in synergy with the polarization measurement by IXPE (Vink et al., 2022). The connection between such observations and the highly detailed radio polarimetric studies, which reflect the much larger regions populated by GeV-energy electrons, can help in following the evolution of nonthermal particles beyond their acceleration sites and in filling out our general picture of the production and evolution of relativistic particles in a supernova remnant.

3.4 Tycho

SNR G120.1 + 1.4, famously known as Tycho, belongs to a class referred to as "Historical Supernovae" due to its association with the supernova explosion SN 1572. Its classification as the

remnant of a normal Type Ia supernova was confirmed with light echos (Krause et al., 2008b). Tycho was one of the first Galactic radio sources identified ("Cassiopeia B"), shown to be separate from the much brighter nearby Cassiopeia A by Hanbury Brown and Hazard (1952), and was only the second radio source, after the Crab, to be identified with a known supernova. That radio synchrotron emission demonstrates the presence of electrons accelerated to GeV energies. Non-thermal X-ray emission was detected up to 25 keV with HEAO-1 (Pravdo and Smith, 1979), indicating for the first time the presence of electrons with TeV energies in Tycho. Following this detection, *Chandra* observations located most non-thermal emission in narrow filaments around Tycho's rim (Hwang et al., 2002; Bamba et al., 2005; Warren et al., 2005). Following that, several non-thermal "stripes" inside Tycho were revealed by follow-up deeper *Chandra* observations (Eriksen et al., 2011). The spacing of these stripes was argued to be of the order of the gyroradius of the highest-energy protons present, giving (for a magnetic field of order 30 μG) proton energies above 10^{15} eV, near the "knee" of the cosmic-ray spectrum around 3 PeV. Subsequent variability studies (Okuno et al., 2020) gave an even higher estimate of ∼100 μG, but the relation to the maximum proton energy relies on several untested assumptions.

Lopez et al. (2015) used *NuSTAR* to perform a spatially resolved spectroscopic analysis of the synchrotron emission and radioactive ^{44}Ti in Tycho's SNR using a deep (∼750 ks) *NuSTAR* observation. The hard (>10 keV) X-rays were found to be concentrated in the southwest of the remnant, where the earlier *Chandra* observation had found the high emissivity "stripes". No evidence was found for ^{44}Ti, and only upper limits were put on its presence. Spatially resolved spectra were fit with a simple model of synchrotron emission from a power-law electron energy distribution with an exponential cutoff, which produces a slower-than-exponential rolloff of emission characterized by the frequency ν_{roll} at which the spectrum has dropped by a factor of 10 below its extrapolation from lower frequencies. Values of rolloff energy $h\nu_{\text{roll}}$ were found to vary over a factor of 5 at different regions around the rim

(Lopez et al., 2015), and were shown to rise as a steep function of the shock velocity obtained from radio expansion measurements (Reynoso et al., 1997).

In addition to Tycho's well-characterized X-ray emission, gamma rays were detected by *Fermi*-LAT at GeV energies (Giordano et al., 2012) and by VERITAS at TeV energies (Acciari et al., 2011). The detection in the TeV range proves that efficient particle acceleration to very high energies is taking place, presumably at the SNR's shock. Whether the gamma rays are due to leptonic or hadronic processes is not clear. The gamma-ray spectrum of Tycho was modeled and found to be consistent with diffusive shock acceleration (DSA) of electrons, in a two-zone leptonic model, (Atoyan and Dermer, 2012), but a hadronic model invoking shock-accelerated cosmic-ray protons was also possible (Berezhko et al., 2013). HEX-P will allow better constraints on high-energy spectral structure which will aid in this discrimination.

3.4.1 Imaging and spectral simulations

Figure 2 shows the broadband (0.7–9 keV) *Chandra* image of Tycho. Regions previously identified with strong nonthermal emission include the thin rims seen around most of the periphery, as well as structures in the west. *Chandra* spectra from the annulus ("rim") and irregular hard-spectrum west region ("W hard") were extracted and fit with power-law models, which were used to simulate images in the LET and HET instruments. Models for the rim were power-laws with photon index $\Gamma = 2.67$ and 3.48 (compared in Figure 3). The same model for the W hard region

was used in each. A purely thermal spectrum of the remainder of the remnant was assumed. The models can clearly be distinguished; the rim is clearly resolvable separately from the W interior region, allowing model discrimination not possible with the *NuSTAR* sensitivity and angular resolution.

Figure 4 shows simulated spectra using XSPEC and the V7 response files for the HET and LET. In all cases, an input power-law index of $\Gamma = 3.0$ was assumed, with normalization based on the *Chandra* image. All spectra are consistent with the data in the *Chandra* band, but with different assumptions about behavior at higher energies. In a 200-ks exposure, parameters of XSPEC simulated straight power-laws can be recovered to within ~5% accuracy, while models with broken power-laws (with $\Delta\Gamma = 3$) do a distinctly poorer job, as quantified by the increase in C statistics. A second set of input models, broken power-law simulated data also steepening by $\Delta\Gamma = 3$ at various assumed energies E_{break}, produce the simulations shown in Figure 4. Fits with the same models recover the two photon indices and E_{break} to within $\approx 2.5\%, \approx 5\%,$ and $\approx 10\%$ for break energies of 20, 30 and 40 keV, respectively. These accuracy levels will enable the detection of hard X-ray variabilities from several prominent X-ray features where particle acceleration is considered to be more energetic and active. These simulations demonstrate the ability of the HET, especially, to characterize the spectral shape in hard X-rays from Tycho, with important implications for the nature of electron acceleration. The detection of steepening, either as smooth curvature or more abrupt spectral breaks, is essential for determining the maximum energies of electrons.
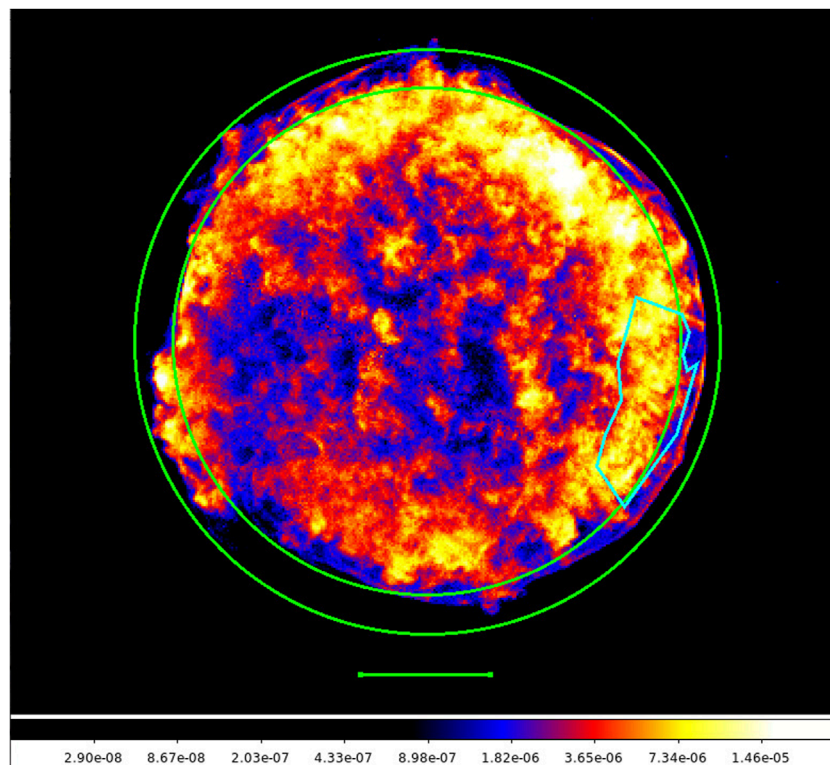
FIGURE 2
Chandra image of Tycho (0.7–9 keV), binned by a factor of 4. Brightness scale is logarithmic; units are erg cm^{-2} s^{-1}. The scale bar has length 2$\prime$. The annulus defines the "rim" region, which contains a high percentage of nonthermal emission. The irregular cyan region in the west has a harder spectrum than most of the remnant. Simulated HEX-P spectra from each, based on *Chandra* data, are shown below.

FIGURE 3
Simulated 100 ks HEX-P images of Tycho's SNR. Input spectral models include a power-law for the W hard interior region, one of two power-law models for the rim region (Γ = 2.67 or 3.48) and a thermal shock model for the remaining interior (parameters not specified as this component contributes negligibly above 8 keV). Units are integrated counts in the indicated energy ranges. **(A)** Rim power-law, Γ = 2.67. **(B)** Rim power-law model, Γ = 3.48. The different rim models can clearly be distinguished.

FIGURE 4
Simulated spectra for a 200-ks observation of Tycho. **(A)** Simulated spectra from parameters given by pure power-law fits to *Chandra* rim data, fit with one pure and three broken power-law models for a 200-ks observation of Tycho. C-statistic values are 398.0 for the power-law fit, and rapidly deteriorate for fits using broken power-law models: 433.7, 662.4, and 2,273.8 for increasingly severe break energies (40, 30, and 20 keV respectively), clearly ruling out the broken power-law models. **(B)** Simulated spectra from parameters given by broken power-law fits to the *Chandra* data, fit with broken power-law models. Input values are recovered to ≈2.5%, ≈5%, and ≈10% accuracy for break energies of 20, 30, and 40 keV, respectively (Cstat values of 418.9, 414.2, and 414.0.

3.5 G1.9 + 0.3

G1.9 + 0.3 is the remnant of the most recent supernova in the Milky Way (Reynolds et al., 2008), with an expansion age of order 140 years (an upper limit to the true age) and (based on hydrodynamic models of the deceleration) a likely explosion date of around 1900 (Carlton et al., 2011). It has an X-ray spectrum dominated by synchrotron emission, with one of the highest rolloff energies of any SNR (over 2 keV; Reynolds et al., 2009). However, thermal emission is detected in small regions, with line widths of

up to 14,000 km s^{-1} (Borkowski et al., 2010), the fastest seen in any Galactic SNR, and consistent with the measured expansion at an assumed distance of 8.5 kpc. The remnant is sufficiently young that particle acceleration (at least in conventional theories) is limited by the remnant age—that is, the maximum electron energy is not set by synchrotron losses, and is the same as the maximum ion energy. This would make G1.9 + 0.3 a unique case where the maximum ion energy can be inferred directly from X-ray observations. The remnant is also the only Galactic SNR still increasing in brightness, at both radio and X-ray wavelengths (Carlton et al., 2011), and it is

expected that the maximum particle energy is also continuing to increase. *NuSTAR* observations (Zoglauer et al., 2015) showed the presence of X-rays out to about 25 keV before the signal was lost in the background. Those observations were unable to discriminate between straight power-laws and power-laws with relatively low (~ 15 keV) cutoff energies, a crucial difference in characterizing the highest-energy electron spectrum. As the simulations of Figure 5 show, HEX-P can resolve this problem. As time goes on, G1.9 + 0.3 provides us with a view of the evolving process of particle acceleration.

3.6 SN 1987A

SN 1987A is the closest supernova known since its explosion 36 years ago in the Large Magellanic Cloud (LMC) located 51 kpc away. While it has been best known for the detection of neutrinos from the supernova event, SN 1987A has exhibited spatial and spectral evolution across a wide range of wavelength bands from radio to X-ray. Shortly after the explosion, X-rays were detected from SN 1987A (e.g., Frank et al., 2016). The X-ray emission, composed of soft and hard components which vary separately, is primarily thermal, considered to arise from the interaction between the expanding shock wave and the surrounding circumstellar material.
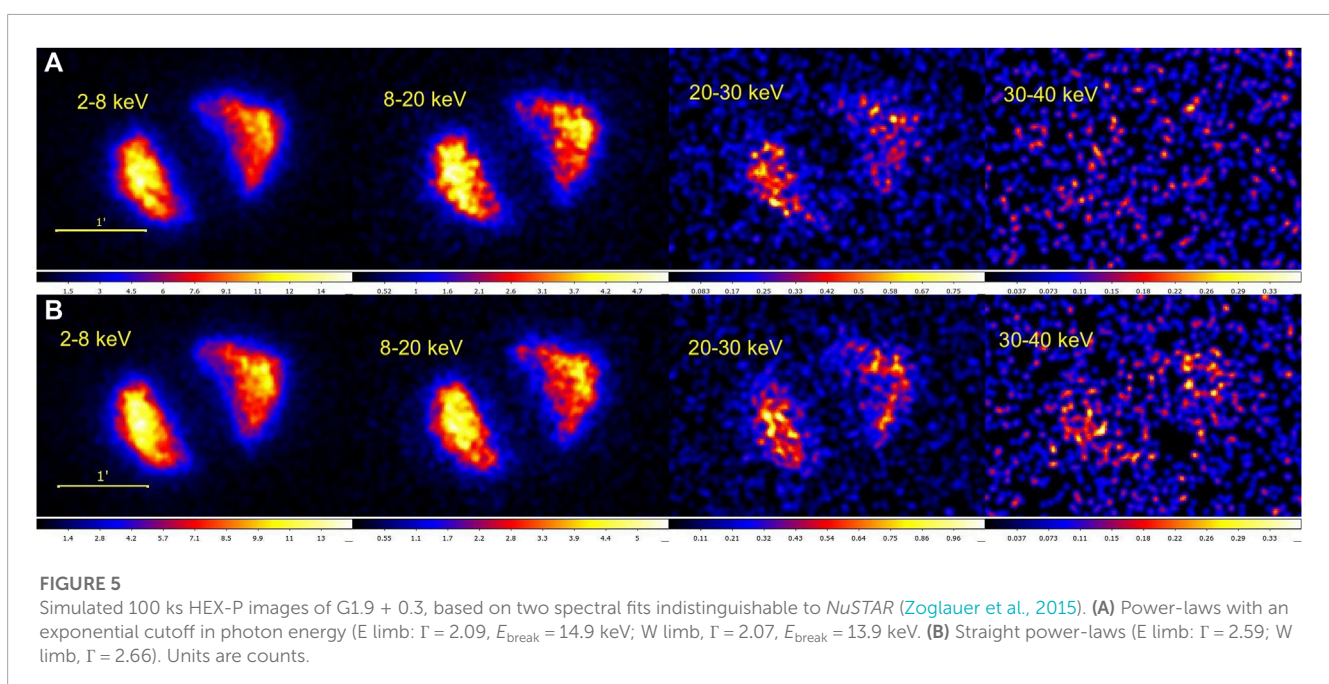
One of the key questions associated with SN 1987A is whether the supernova left a neutron star or black hole. Some hints on the presence of a NS at the core were suggested by recent ALMA radio and *NuSTAR* hard X-ray observations. ALMA detected a bright spot, suggesting that local dust is being heated by the NS's thermal emission (Cigan et al., 2019). *NuSTAR* observed non-thermal X-ray emission above 10 keV, suggesting the presence of a PWN (Greco et al., 2021). However, despite the *NuSTAR* observations with 3.3 Ms total exposure, the detection of a PWN component is still under debate (Alp et al., 2021; Greco et al.,

2022), and more sensitive hard X-ray observations are required for making a firm detection of the putative PWN. A contribution to the hard X-rays from synchrotron emission from electrons accelerated in the SN blast wave cannot be ruled out, as the blast wave radius is smaller than an arcsecond. Note that only the hard X-ray band above 10 keV can be observed from the core region due to severe photo-absorption by heavy-element ejecta (Alp et al., 2018). HEX-P's energy coverage from 0.2 to 80 keV will be essential for fully characterizing both thermal and non-thermal X-ray components. Figure 6 shows simulated HEX-P spectra of SN 1987A. While SN 1987A is a point source to HEX-P as it is for *NuSTAR*, HEX-P's better angular resolution means smaller background in a resolution element, enhancing the sensitivity to unconfirmed non-thermal emission above 10 keV compared to *NuSTAR*.

Since the multi-wavelength emission components from SN 1987A are expected to vary on year timescales, as seen over the last 35 years, HEX-P will be able to provide a broadband and high-resolution X-ray view of how both thermal and non-thermal X-ray emission appears and evolves in the 2030s. Since CTA selected the LMC survey as one of CTA's key science projects (Cherenkov Telescope Array Consortium, 2023), HEX-P and CTA will jointly reveal hard X-ray and TeV emission from synchrotron and inverse-Compton radiation associated with the SNR and possibly emerging PWN, respectively.

4 Pulsar wind nebula

A pulsar wind nebula (PWN) is a bubble of non-thermal radiation from a magnetized, primarily electron/positron plasma which is supplied by an energetic pulsar. The confinement of the initially relativistic pulsar wind by its environment results in a termination shock. Particles are thought to be accelerated to high
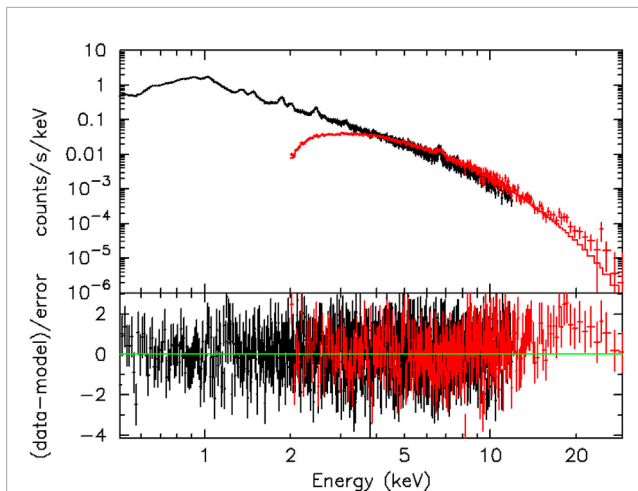

FIGURE 5
Simulated 100 ks HEX-P images of G1.9 + 0.3, based on two spectral fits indistinguishable to *NuSTAR* (Zoglauer et al., 2015). **(A)** Power-laws with an exponential cutoff in photon energy (E limb: $\Gamma = 2.09$, $E_{break} = 14.9$ keV; W limb, $\Gamma = 2.07$, $E_{break} = 13.9$ keV. **(B)** Straight power-laws (E limb: $\Gamma = 2.59$; W limb, $\Gamma = 2.66$). Units are counts.

FIGURE 6
Simulated *HEX-P* LET (black) and HET (red) spectra of SN 1987A assuming a 300 ks exposure. The input spectral parameters for the three thermal components ($kT_1 = 0.48, kT_2 = 0.96, kT_3 = 3.2$ keV) and a power-law component ($\Gamma = 2.6$) were adopted from the *Chandra, XMM* and *NuSTAR* observations obtained in 2020 (Greco et al., 2022). The simulated *HEX-P* spectra are fit with the thermal components only to illustrate the presence of the non-thermal emission above 10 keV. The non-thermal component is detected with 7σ significance and its photon index is well constrained to $\Gamma = 2.4^{+0.2}_{-0.1}$, much improved from the 2020 *NuSTAR* observation with 350 ks exposure ($\Gamma = 2.6^{+0.7}_{-1.8}$) (Greco et al., 2022).

energies in the shock and flow and diffuse outward to produce a PWN. PWNe are expected to evolve through three phases: an initial phase in which the young PWN expands into the cooled expanding ejecta of its natal SNR; a second phase in which the SNR's reverse shock wave has returned toward the center and recompressed the PWN, distorting it and perhaps moving it off-center in the SNR; and a third phase, after the pulsar has either left the SNR or outlived it, and its wind is interacting with undisturbed ISM. Since pulsars are typically born with substantial kick velocities, in this third phase they are normally moving supersonically in the ISM and their PWN is in the form of a bow-shock nebula. Most modeling has been done for the earlier stages. Kennel and Coroniti (1984a; Kennel and Coroniti, 1984b) modeled the Crab Nebula with a spherically symmetric magnetohydrodynamic model assuming pure advection of particles behind the termination shock, successfully explaining its basic features. Later detailed MHD simulations have reproduced many features of the X-ray morphology of the Crab Nebula, including small-scale structures such as jets and tori (e.g., Del Zanna et al., 2004; Komissarov and Lyubarsky, 2004), features found in many other PWNe (Ng and Romani, 2004, and references therein). While these MHD models capture the main properties of the Crab Nebula, they do less well in describing properties common in other PWNe that the Crab does not share, such as uniformly steepening spectra with distance from the pulsar. In general, there is a great deal more to be learned about the diversity of PWN phenomenology that the MHD models cannot answer. TeV and even PeV photons are observed in PWNe (Cao et al., 2021), meaning that they accelerate electrons to even higher energies. These particles can escape from the PWNe and could contribute significantly to

the flux of energetic electrons and positrons detected on Earth (e.g., Abeysekara et al., 2017a).

Particle acceleration in PWNe is thought to occur at the relativistic termination shock via DSA or magnetic reconnection as demonstrated by particle-in-cell (PIC) simulations (e.g., Sironi and Spitkovsky, 2009; Sironi and Spitkovsky, 2014). However, it is still unclear to what energy the particles are accelerated, how they evolve as they flow and diffuse, and how they escape from the PWNe. These can be addressed by high-quality X-ray and gamma-ray data. In particular, synchrotron X-rays probe the highest-energy electrons, as their inverse-Compton gamma-ray emission is suppressed by the Klein-Nishina effect. Sensitive X-ray and gamma-ray observatories have helped to address these questions during the previous 2 decades, but many important questions remain unanswered. We list questions (1)–(3) as shown below.

4.1 Important questions to address on PWN physics

4.1.1 Particle acceleration in relativistic shocks

Numerous PWNe emit TeV (even PeV) photons, implying that there must be very energetic particles accelerated at their termination shocks or elsewhere. Indeed, half of the unidentified TeV sources discovered in H.E.S.S. Galactic plane surveys are now categorized as middle-aged or old PWNe (H.E.S.S. Collaboration, 2018), and half of the sources listed in the first LHASSO source catalog are linked with pulsars and/or PWNe (Cao et al., 2023). Most of them are theoretically compatible with being powered by a pulsar (de Oña Wilhelmi et al., 2022). Because the energy distribution of the particles is imprinted in their radiation spectrum, accurate measurements of PWN spectra will give us clues to particle acceleration processes in relativistic shocks. Although PeV-energy particles are already detected in the Crab Nebula, an important question is whether or not other PWNe can generally accelerate particles to such energies (i.e., constitute leptonic PeVatrons). As in other sources, Klein-Nishina suppression of inverse-Compton scattering from the highest-energy electrons means that their energy distribution, up to those highest energies, is best probed not by gamma rays but by sensitive high-energy X-ray observations of synchrotron emission. Modeling of X-ray and gamma-ray data of various PWNe has given maximum particle energies of ~PeV not only in young sources ($\lesssim 10^4$ years; e.g., Torres et al., 2014; Abdelmaguid et al., 2023) but also in middle-aged ones (~10^4–10^5 years; e.g., Burgess et al., 2022; Park et al., 2023a; Woo et al., 2023). While these estimates depend strongly on B within the PWN (an electron of energy E emits its peak synchrotron power at a photon energy $h\nu_m \propto E^2 B$), broadband spectral-energy-distribution (SED) models can constrain B, especially if spectral features such as spectral breaks or cut-offs, spatial variation of the spectrum, and/or energy-dependent morphology are measured. An independent B estimation is possible if the seed-photon radiation energy density $u^\star$ in the PWN region is known, since $P_{synch}/P_{IC} = u_B/u^\star$ (in the Thomson regime), where $u_B \equiv B^2/8\pi$ is the energy density in magnetic field. The state-of-the-art code GALPROP (Porter et al., 2022, and references therein) provides models for Galactic distributions of cosmic rays as well as of the

interstellar radiation field.[1] The latter provides models for $u^\star$ within the Galaxy, thereby allowing an independent estimation of B in PWNe. High-quality X-ray data will facilitate measurements of the aforementioned spectral and spatial features with high precision, and these, combined with improved $u^\star$ estimations, will improve our understanding of particle acceleration processes in PWNe.

4.1.2 Particle injection into the interstellar medium

The origin of the cosmic-ray positron flux detected on Earth at energies higher than a few GeV is a longstanding puzzle (e.g., Aguilar et al., 2019), and it was suggested that nearby pulsars and their PWNe are an important source of these particles (e.g., Cholis and Hooper, 2013; Della Torre et al., 2015; Xi et al., 2019; Manconi et al., 2020). Radiative energy losses restrict possible sources of the highest-energy terrestrial cosmic-ray leptons with $E \gtrsim 1$ TeV to within about 1 kpc, but studying numerous PWNe in a larger volume can aid in understanding energetic leptons within the Galaxy. After being accelerated at the relativistic termination shock of the pulsar wind, leptons evolve in the PWN under radiative and advective cooling (e.g., Reynolds, 2009; Van Etten and Romani, 2011; Park et al., 2023b). Young systems are expected to efficiently confine the nebular plasma, and in general they might not be an efficient source of energetic cosmic-ray electrons in the Galaxy, since their electrons rapidly lose energy to radiation via synchrotron emission in the strong magnetic fields typical of such objects. However, we do have direct evidence of an efficient escape of particles in the outer medium from middle-aged and more evolved systems (see e.g., Olmi and Bucciantini, 2023, for a recent review of systems in different phases and their observational signatures).

A first clear indication is TeV halos seen around old PWNe (e.g., Yüksel et al., 2009; Bamba et al., 2010; Sudoh et al., 2019; Abeysekara et al., 2017a; H.E.S.S. Collaboration, 2023). These TeV halos are likely due to the sum of all particles which have escaped over time during the lives of the PWNe. A second piece of evidence is the presence of extended (from 1 to several pc), asymmetric and collimated X-ray features protruding from some high-speed bow shock PWNe (e.g., Kargaltsev et al., 2017), showing a strong misalignment with respect to the pulsar direction of motion. These intriguing features can be explained as formed by energetic particles leaving the PWN, advected away along the ambient magnetic field lines (Olmi and Bucciantini, 2019). Some degree of amplification of the ambient field is necessary to explain the observed emission as due to synchrotron radiation (Bandiera, 2008), possibly produced by the particles themselves. An excellent example is the Lighthouse PWN (IGR J11014−6103) powered by the old 120 kyr pulsar PSR J1101−6101 (Halpern et al., 2014). It shows a ~6′ long and bright collimated outflow to the west (Pavan et al., 2016), with evidence for spectral evolution along the feature in the combined observations from *Chandra* and *NuSTAR* (Klingler et al., 2022). The possibility of investigating the spectrum of such features in the very extended energy band of HEX-P, and with its angular resolution, is a key ingredient to understand not only the properties of escaped particles (and thus of the PWN) but also how they interact with the ambient medium, with important consequences

for our understanding of the physics of transport and diffusion in the vicinity of sources. All these points are then intimately connected both with point (1)—how and to what energy particles are accelerated at the pulsar wind termination shock—and the following point (3)—how particle acceleration and escape change as the PWN evolves.

4.1.3 Co-evolution of the PWN and its SNR

The evolution of a PWN is tightly linked to that of its host SNR. The entire evolutionary history affects the particle energy distribution within the PWN today, which is imprinted in the emission SED. The size and expansion speed of PWNe provide additional information on the co-evolution since the PWN expansion is influenced by, first, the surrounding SNR ejecta, and later by the reverse shock (e.g., Hattori et al., 2020). Effects of PWN/SNR co-evolution (e.g., Bandiera et al., 2020; 2023) are particularly important in understanding cosmic-ray electrons since we need to consider the entire history of particle injection by PWNe to compare with cosmic rays detected today. The co-evolution is very complex, and hydrodynamic (HD) simulations have been carried out to study the dynamic evolution of PWN-SNR systems (e.g., Bucciantini et al., 2003; Kolb et al., 2017). In these works, the broadband spectral properties of the PWNe have not been considered. Gelfand et al. (2009) developed a dynamic and radiative evolution model by treating the PWN-SNR co-evolution in a semi-analytic way (Reynolds and Chevalier, 1984), in a one-zone model with spherical symmetry. This evolutionary PWN model has successfully fit the SED, size, and expansion speed of some PWNe (e.g., Abdelmaguid et al., 2023), and the model-inferred properties of the SN and SNR seem to agree reasonably well with other SNR evolution models (e.g., HD simulations). While PWN evolution models are very useful for understanding PWN physics and can provide a supplementary tool for understanding SNR physics, the models have many covarying parameters, and one-zone models fail to capture the obvious inhomogeneities and morphological complexities of almost all PWNe. Moreover, recent higher-resolution HD studies (e.g., Bandiera et al., 2020; 2023) found deviations from the prescriptions used for the dynamic evolution in the radiative evolution model of Gelfand et al. (2009). These deviations may be manifest in the spatially-varying emission properties and can have a significant impact on the highest-energy particles. Measurements of the spatially-integrated SED, size, and expansion speed are certainly insufficient for studying the co-evolution in detail and precise measurements of the PWN properties (e.g., spatially-resolved spectra) are necessary to enrich our understanding of PWNe and SNRs.

4.2 HEX-P contribution to PWN physics

Accurate characterizations of the PWN emission properties are crucial to address the aforementioned questions. Question 1 requires sensitive measurements of high-energy X-ray spectra of PWNe. For Questions 2 and 3, accurate measurements of spatially-resolved emission properties are necessary, along with an emission model that takes into account the temporal and spatial evolution of particles within the PWN. While existing X-ray observatories have helped address these questions, their sensitivity to faint emission

---

1 https://galprop.stanford.edu/code.php?option=theory

and to spectral detail is not yet sufficient to provide firm answers. *Chandra* and *XMM* have measured PWN images and spectra in great detail, but their lack of sensitivity above 10 keV precludes detailed investigation of the most energetic electrons. While this could be supplemented by *NuSTAR*'s hard X-ray data (see Reynolds, 2016; Mori et al., 2021), cross-calibration uncertainties between the observatories cause some problem (e.g., Madsen et al., 2015a; 2017a; Hattori et al., 2020; Abdelmaguid et al., 2023). In addition, the low angular resolution (60″ HPD), limited effective area, and strong and inhomogeneous backgrounds of *NuSTAR* (e.g., Wik et al., 2014; Madsen et al., 2017b) have been a concern for measurements of spatially-integrated and resolved spectra of PWNe above 20 keV.

The HEX-P observatory can revolutionize our studies of PWNe. The broadband coverage of the combined LET and HET instruments provides a large lever arm for spectral measurements, and thus the properties of emission by highest-energy electrons, which may be manifested as a spectral cutoff, can be well measured. Figure 7 shows detectability of a strong spectral break at E_{brk} (broken from $\Gamma_l = 2$ to $\Gamma_h = 5$ as was suggested for 3C 58; An, 2019), simulated for a generic $R = 3'$ PWN assuming a 100 ks observation with HEX-P. Note that other gradual cut-off shapes, e.g., exponential cutoffs at E_{cut}, are more easily detected because the spectral shape starts to change at low energies as compared to the broken power-law case. We also mark fluxes of some bright PWNe in the figure for reference. The simulations show that we can detect a spectral break up to 50 keV if the source is bright (e.g., $F \geq 10^{-10}$ erg s^{-1} cm^{-2} in the 2–10 keV band) and if its spectrum indeed exhibits a spectral cutoff. This experiment will be particularly useful for some PWNe in which a spectral curvature or cutoff was measured (e.g., Crab, G21.5−0.9, PSR J1400−6325, and PSR J1813−1749; Madsen et al., 2015a; Nynka et al., 2014; Hitomi Collaboration et al., 2018; Renaud et al., 2010; Bamba et al., 2022; Hattori et al., 2020) or suggested (e.g., 3C 58 and N157B; An, 2019; Bamba et al., 2022). This will help address Question 1. Note that *NuSTAR* data have some systematic uncertainty

due to the inhomogeneous background which is very difficult to assess for diffuse PWNe. HEX-P, in addition to having twice the effective area and lower backgrounds, would not suffer from such inhomogeneous background. Hence the improvement can be substantial.

In studying PWN emission using an evolutionary model, it is crucial to measure the emission SED as precisely as possible. This can provide additional information to break parameter covariance of the evolutionary model since the SED shape changes depending sensitively on the cooling history of the particles (e.g., Gelfand et al., 2009). In this regard, the broadband coverage of LET + HET of HEX-P is particularly helpful. The right panel of Figure 7 shows HEX-P's sensitivity to a small degree of curvature in the emission spectrum investigated using the `logpar` model in *XSPEC* ($dN/dE = K(E/E_p)^{-a-b\log(E/E_p)}$ with $E_p = 5$ keV) for $R = 3'$ PWN emission. This value of the pivot energy E_p was chosen as it is near the center of HEX-P's full LET + HET bandpass, thus posing the most stringent test for sensitivity to departures from a power-law. Simulations of a 100-ks exposure show that HEX-P will be able to measure a shallow curvature with $b < 0.1$ (corresponding to ~20% SED change over the 0.3–80 keV band) if the source flux in the 2–10 keV band is $\geq 10^{-11}$ erg s^{-1} cm^{-2}. This is sufficient for measuring spectral breaks detected in some young PWNe, which will provide important clues to the particle acceleration mechanisms and PWN-SNR co-evolution. In particular, Klingler et al. (2022) found in outflow regions of the Lighthouse PWN that the soft X-ray (*Chandra*) spectra are discrepant with the hard X-ray (*NuSTAR*) ones, implying that the effects of particle evolution (e.g., cooling) are best seen at >8 keV. However, this could not be confidently stated because of cross-calibration issues and non-uniform background in the *NuSTAR* data. HEX-P observations will help to clarify this since the suggested spectral curvature is large enough for detection, and can shed light on the properties of the particles escaping the PWN and their effect on the ambient medium (Question 2).
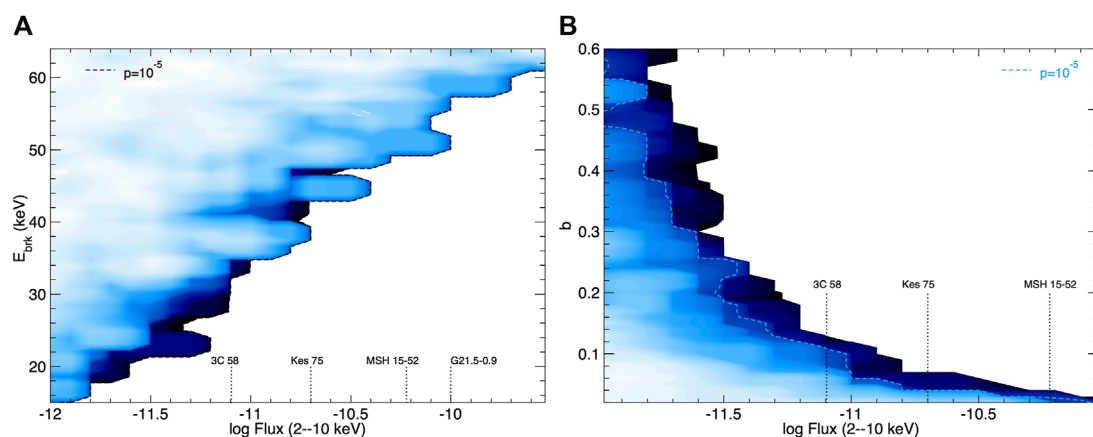

FIGURE 7
Results of HEX-P simulations of a generic $R = 3'$ extended PWN. **(A)** *F*-test probability contours between a power law (PL) and a broken power-law (BPL) model. Simulated HEX-P data (100-ks) for a BPL spectrum having $\Gamma_l = 2$ and $\Gamma_h = 5$ at break energy E_{brk} are fit by a BPL and a PL, and the addition of the break was tested using the *F* statistic. **(B)** Same as the left, but the simulations were carried out for a `logpar` model with varying *b* (see text). The vertical dashed lines mark fluxes of some young and bright PWNe: 3C 58 (An, 2019), Kes 75 (Gotthelf et al., 2021), MSH 15–52 (An et al., 2014), and G21.5–0.9 (Nynka et al., 2014).
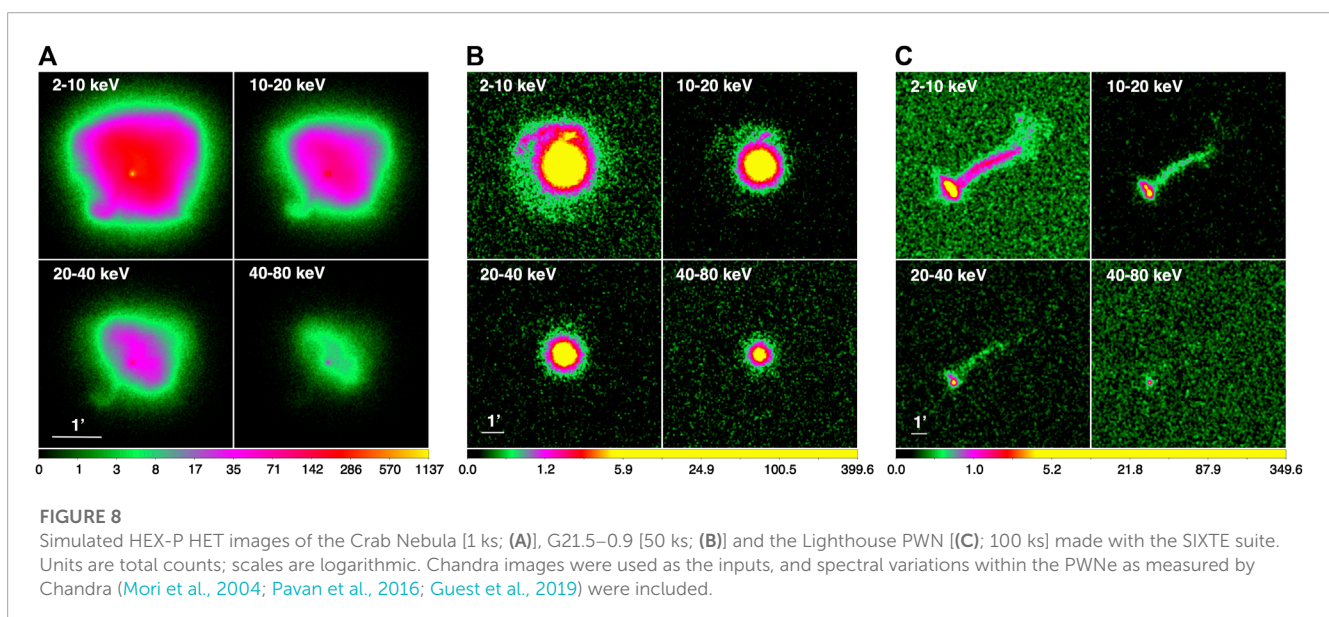
HEX-P will also allow measurements above 10 keV of faint emission in the outer regions of extended (and evolved) PWNe. This will help to characterize synchrotron burn-off effects as well as particle flow near the outer boundary of the PWNe, and to provide new insights into the evolution of PWNe after their young phase (Question 3). We can then estimate the amount and spectrum of electrons that escape from the X-ray PWN and propagate to larger TeV emission regions. With the advent of high-resolution TeV observatories (e.g., CTA), the HEX-P data will tell us about how the electron spectrum evolves as electrons propagate from the X-ray PWN to the TeV emission region, and eventually to the interstellar medium. This will help address Question 2. In our 100-ks simulations of a HEX-P observation of a $R = 4'$ PWN, we found that we could measure the photon index of an annular region with the inner and outer radii of $3'$ and $4'$ to within 0.1 if the 2–10 keV flux is higher than 3×10^{-13} erg s^{-1} cm^{-2}. In other PWNe, the injection regions may be too faint for accurate measurement of the spectrum. These faint regions can still be identified by images, and our simulations of HEX-P observations for a hypothetical PWN suggest that faint source emission within an annular region with the inner and outer radii of $4'$ and $4.25'$ (i.e., width of $15''$) can be detected with 3σ confidence if the flux is higher than 3×10^{-14} erg s^{-1} cm^{-2}.

4.3 HEX-P simulations for the Crab Nebula, G21.5−0.9, Lighthouse PWN and G0.9 + 0.1

HEX-P plans to observe the Crab, G21.5−0.9, Lighthouse PWN and G0.9 + 0.1 in the primary science program. The improved PSF of HEX-P HET will resolve substructures in the sources much better than *NuSTAR* could. In addition, HEX-P's large effective area will allow more accurate spectral characterization of the sources. Figure 8 shows simulated images of the sources made with the SIXTE suite. Compared to *NuSTAR*'s images of the sources (Nynka et al., 2014; Madsen et al., 2015a; Klingler et al., 2022), the morphologies of the PWNe are much better resolved.

The torus and jets of the Crab Nebula and the northern spur and eastern limb of G21.5−0.9 were seen by *NuSTAR* only after deconvolving the PSF from the images, and thus their spectra could not be measured. The HET of HEX-P can resolve those structures as in the simulated images (Figure 8), allowing spectral measurements. Nonthermal emission from the northern spur and the eastern limb of G21.5−0.9 that were suggested based on deconvolved images (Nynka et al., 2014) can be better characterized by HEX-P observations. This also applies to other sources in which *NuSTAR*'s resolution was insufficient to resolve various structures in them, requiring deconvolution (e.g., G11.2−0.3; Madsen et al., 2020).

The Lighthouse PWN is particularly intriguing thanks to its long (∼6′) and misaligned tail, which connects to a diffuse emission region (Pavan et al., 2016). The morphological change from a collimated jet to a diffuse region in this PWN can tell us much about electron injection from the old PWN into the ISM. The *NuSTAR* measurement of the spectrum of the diffuse region ($\Gamma = 2.21 \pm 0.08$) was discrepant with the *Chandra* result ($\Gamma = 1.74 \pm 0.05$) (Klingler et al., 2022), suggesting that the electrons had experienced strong cooling. However, this was uncertain because of unknown systematic effects in the data, e.g., cross-calibration between the observatories and inhomogeneous background in the *NuSTAR* data (the latter was a particular concern; see Klingler et al., 2022). Our HEX-P simulations for a 100-ks observation of the Lighthouse PWN, based on the previous *NuSTAR* results, found that HEX-P would be able to detect the diffuse emission at ≥6′ up to ∼20 keV (Figure 8) and to measure its spectrum accurately, e.g., constraining Γ_X to within 0.04. This will provide sufficient sensitivity for discriminating between the hard vs. soft injection spectra as measured by *Chandra* and *NuSTAR*. More importantly, HEX-P data (LET + HET) will not suffer from systematic effects due to cross-calibration across the 0.2–80 keV band or to inhomogeneous background. Hence, HEX-P observations of the Lighthouse PWN will considerably improve the *Chandra* and *NuSTAR* measurements, and thereby provide

FIGURE 8
Simulated HEX-P HET images of the Crab Nebula [1 ks; **(A)**], G21.5−0.9 [50 ks; **(B)**] and the Lighthouse PWN [**(C)**; 100 ks] made with the SIXTE suite. Units are total counts; scales are logarithmic. Chandra images were used as the inputs, and spectral variations within the PWNe as measured by Chandra (Mori et al., 2004; Pavan et al., 2016; Guest et al., 2019) were included.

crucial clues to how the PWN electrons are injected into the ISM.
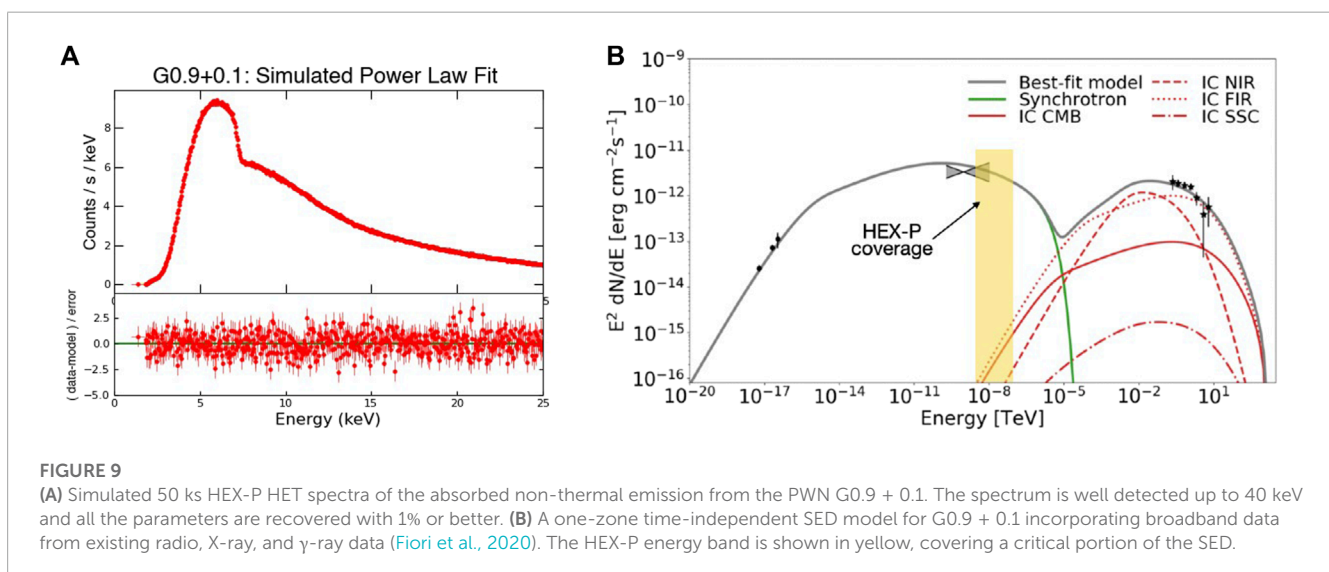
G0.9 + 0.1 is a composite-type supernova remnant (SNR) and pulsar wind nebula (PWN) located only one degree from the Galactic Center, long studied in the X-ray regime. As the system is quite young with a spin-down age of τ_c = 5.3 kyr (Camilo et al., 2009), the SNR shell has not interacted with the $d \sim 2'$ PWN core (Helfand and Becker, 1987) leaving the nebula an ideal candidate for probing the physical mechanisms responsible for accelerating high-energy particles. X-ray observations below 10 keV by *Chandra* (Gaensler et al., 2001) and *XMM* (Porquet et al., 2003; Holler et al., 2012) reveal prototypical non-thermal emission with a radially dependent power-law index, a signature of PWN synchrotron cooling. Despite its young age and energetic pulsar, the nebula has coincident γ-ray emission (Aharonian et al., 2005; Adams et al., 2021) that is relatively underluminous for its pulsar luminosity, making this an interesting target to probe high-energy particle acceleration. *NuSTAR* observations were able... were able to detect the non-thermal PWN emission up to 30 keV. However, stray light caused by the proximity to the Galactic Center reduces the quality of the data and the spectral parameters are only moderately constrained. HEX-P simulations of G0.9 + 0.1 show a significant improvement in the >10 keV range (Figure 9A). Broadband studies with multi-wavelength SEDs have attempted to probe the underlying acceleration processes. Several one-zone time-dependent leptonic models (e.g., Fiori et al., 2020) have been adopted with various constraints applied to input parameters, while other models explored lepto-hadronic scenarios (Holler et al., 2012), multiple zones, or incorporated significant adiabatic cooling (Tanaka and Takahara, 2011). While these complex models fit the available data, they often leave crucial parameters, such as the injected electron spectral index, unconstrained. HEX-P provides critical coverage at the energy band where the majority of models predict a turnover in the SED curve (Figure 9B). HEX-P data added to broadband SED analysis will provide a deeper understanding of the extreme particle acceleration processes within PWNe.
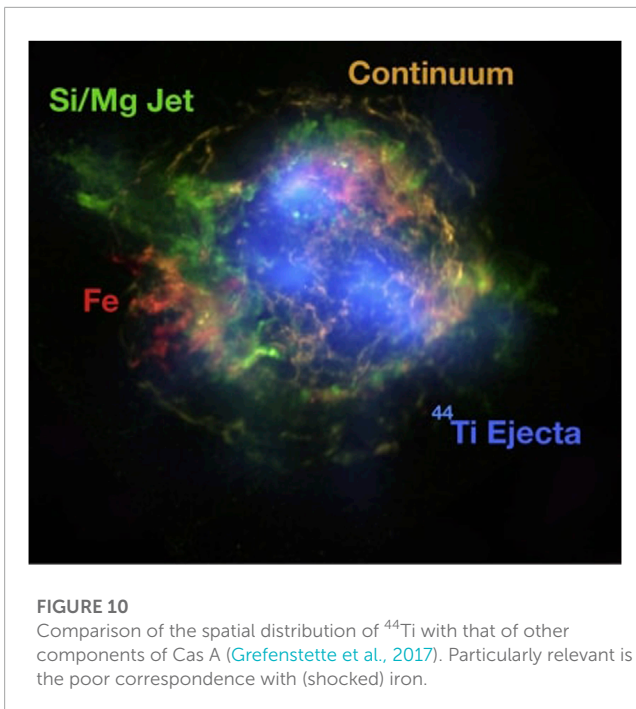
4.4 Summary

The broadband coverage, superior angular resolution, and low background of HEX-P HET will provide significant improvement in our understanding of PWNe. In addition to the spectral improvement, the HET of HEX-P will measure the morphologies of PWNe in greater detail compared to *NuSTAR* as presented in Figure 8. Hard X-ray emission from substructures (e.g., torus, jets, and knots) in PWNe will be better probed. HEX-P will observe the Crab Nebula and G21.5−0.9 as calibration targets, and these observations will provide unprecedented data for these two young and bright PWNe, allowing precise SED studies. In addition, a 100 ks HEX-P observation of the Lighthouse PWN will measure the spectra of the outflow regions out to $\geq 5'$ without systematic effects due to inhomogeneous background. This will probe how the electrons in the outflows evolve and merge into the ISM.

5 Nucleosynthesis in the galaxy

While HEX-P can revolutionize the study of hard X-ray nonthermal continua from particle accelerators, the spectral region above 10 keV holds little information on thermal line emission. However, HEX-P can make a major improvement in line spectroscopy of another sort: radioactive decay of freshly synthesized unstable isotopes from supernovae or from double neutron-star mergers. In supernovae, the well-known hard X-ray nuclear decay lines at 68 and 78 keV emitted in the decay chain of ^{44}Ti contain invaluable information on the synthesis of iron-group elements. One of the most important results from *NuSTAR* was the detection of these spectral lines from SN 1987A, and more significantly, their imaging as well, from Cas A. Unlike lines from collisionally ionized iron which must be shocked to high temperatures, these lines are emitted independent of temperature, so show the presence of titanium both before and after interaction with the reverse shock in a supernova interior. The imaging of ^{44}Ti in Cas A violated the widely held expectation that its


FIGURE 9
(A) Simulated 50 ks HEX-P HET spectra of the absorbed non-thermal emission from the PWN G0.9 + 0.1. The spectrum is well detected up to 40 keV and all the parameters are recovered with 1% or better. **(B)** A one-zone time-independent SED model for G0.9 + 0.1 incorporating broadband data from existing radio, X-ray, and γ-ray data (Fiori et al., 2020). The HEX-P energy band is shown in yellow, covering a critical portion of the SED.

FIGURE 10
Comparison of the spatial distribution of ^{44}Ti with that of other components of Cas A (Grefenstette et al., 2017). Particularly relevant is the poor correspondence with (shocked) iron.

FIGURE 11
Distribution of ^{26}Al, ^{44}Ti, ^{48}Cr, ^{56}Ni, ^{60}Fe, and total Fe as a function of mass. Like ^{56}Ni and ^{48}Cr, ^{44}Ti traces the innermost ejecta. Of the isotopes probing the innermost ejecta, ^{44}Ti is uniquely observable in young supernova remnants.

distribution would mirror that of ^{56}Ni and its stable decay product ^{56}Fe. The famous *NuSTAR* image (Figure 10) shows fairly poor correspondence. However, even *NuSTAR*′s 2.4 Ms integration time was not sufficient to fully characterize the distribution at lower flux levels, and the spatial resolution, far poorer than that of the Fe Kα image produced by Chandra, did not permit more detailed examinations of Ti/Fe ratios. Both these limitations will be much less severe with HEX-P, which can improve on the *NuSTAR* detections, but also search for ^{44}Ti from other young supernova remnants (both core-collapse and Type Ia, though significant titanium production in SNe Ia probably requires high degrees of explosion asymmetry). Most excitingly, HEX-P could examine a sufficiently nearby binary neutron star merger event, with the prospect of obtaining information inaccessible to optical or soft X-ray instruments.

5.1 ^{44}Ti line emission from young SNRs

In a supernova explosion, ^{44}Ti is produced in the innermost ejecta (either in the convective region or just above it; Magkotsios et al. (2010); Fryer et al. (2023)) and is one of the most direct tracers of the supernova engine (Figure 11). ^{44}Ti production is extremely sensitive to the strength of the shock and can probe explosion asymmetries (Magkotsios et al., 2010; Vance et al., 2020). But the Cas A observations (Figure 10) highlighted issues with our understanding of the explosion mechanism.

^{44}Ti provides an ideal probe of the supernova engine. Because ^{44}Ti is produced near the engine, it traces the explosion asymmetries caused by this engine. *NuSTAR* observations of the ^{44}Ti distribution provided the most direct evidence to date supporting the convective-engine paradigm behind core-collapse
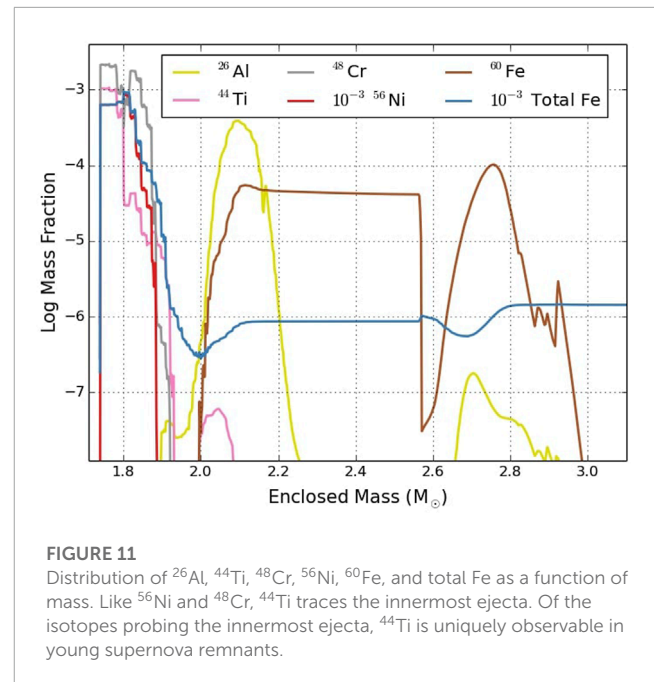
supernovae (Grefenstette et al., 2014; 2017; Wongwathanarat et al., 2017; Vance et al., 2020). More precise maps of the ^{44}Ti distribution will further constrain the asymmetries in the models. In addition, the amount of ^{44}Ti produced and the ratio of ^{44}Ti to iron or other iron-peak elements provide further probes of the engine and, ultimately, the nuclear physics producing these yields.

5.1.1 Cas A

Cas A provides the only example of spatially resolved ^{44}Ti emission from a young SNR (Grefenstette et al., 2014; Grefenstette et al., 2017; Figure 10). The distribution of the ^{44}Ti already provides constraints on the asymmetries of the explosion. When these observations were obtained, constraints on the iron and other iron-peak elements were limited to iron located through X-ray emission from highly ionized states, meaning that only material having passed through the reverse shock could be observed. The long *NuSTAR* observation (2.4 Ms) was limited by spatial resolution and by background; it is possible that fainter ^{44}Ti emission could be detected and would provide quantitative measures or limits on the local Ti/Fe ratio, especially for redshifted features where both the 68 and 78 keV spectral lines could be observed. Combining more detailed HEX-P maps with recent JWST observations of this remnant (measuring unshocked iron) will allow scientists to study details of both the shock properties and the nuclear physics. Figure 12 shows the simulated HEX-P image in 67–69 keV using Chandra's Fe Kα map as a guide for the ^{44}Ti map. We emphasize that, as Figure 10 graphically demonstrates (Grefenstette et al., 2014; 2017), the ^{44}Ti distribution in Cas A does not trace the distribution of Fe Kα. Currently, the only available ^{44}Ti map is from the *NuSTAR* observations at a resolution of ~1′, so to exhibit the effect of HEX-P's superior angular resolution, we use the *Chandra* Fe Kα image as input, knowing that the resultant simulated image is a demonstration only (compare the resolution of Figure 12 to the *NuSTAR* image Figure 10). However,
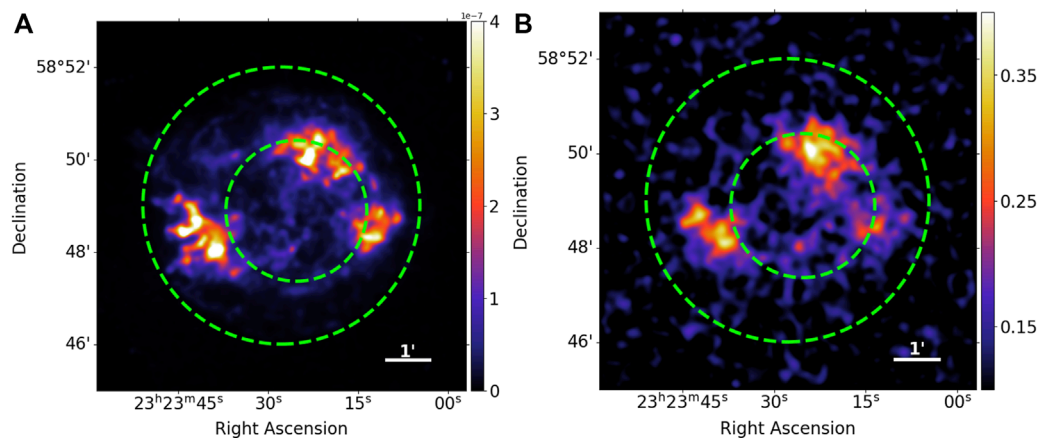
FIGURE 12
(A) Chandra Fe Kα map (6.54−6.92 keV). **(B)** Simulated HEX-P image of ^{44}Ti emission from Cas A (67−69 keV) for 1.5 Ms exposure using the Chandra Fe Kα map as the input image. The green dotted lines mark the forward (outer ring) and reverse (inner ring) shock, respectively. This image is merely to demonstrate HEX-P's high spatial resolution, as we have no access to the "true" distribution of ^{44}Ti.

the integrated flux in the simulated image is that measured by *NuSTAR*.

5.1.2 Other possible sources

The 85-year mean life of ^{44}Ti means that only SNRs less than a few hundred years old will be detectable sources. Our primary target list includes (in addition to Cas A) two such objects, SN 1987A, and Tycho's SNR. SN 1987A was detected by *NuSTAR* in a 2.6 Ms exposure, with a flux in the 68 keV line of $(3.5 \pm 0.7) \times 10^{-6}$ photons cm^{-2} s^{-1}, at a mean epoch of 27 years after the SN. In our proposed 300 ks HEX-P exposure, and assuming an observation year of 2029, we estimate about 10% of the signal, which should allow a detection, though not an improvement over *NuSTAR*. Type Ia supernovae such as the one that produced Tycho are not expected to synthesize large masses of ^{44}Ti, but asymmetric explosion models have predicted values of $(1–3) \times 10^{-5}$ $M_\odot$ (Maeda et al., 2010), or about 10% of the mass of 1.4×10^{-4} $M_\odot$ inferred for Cas A (Grefenstette et al., 2017). A similar scaling of the flux from Cas A to the distance (2.3 kpc; Chevalier et al., 1980) and age (451 years) of Tycho, and assuming 0.1 times the ^{44}Ti mass of Cas A, gives a line flux of about 6% of that of Cas A.

In addition to Cas A, two other remnants of core-collapse supernovae have ages of order a few hundred years, as inferred from expansion measurements. Kes 75 (G29.7-0.3), a combination shell SNR/PWN/pulsar system, has an age of 480 ± 50 years (Reynolds et al., 2018). At a distance of 5.8 kpc, it could produce a detectable signal. Again scaling the observed line flux from Cas A to the distance and age of Kes 75, we estimate a flux of about 7% of that of Cas A. Similarly, the remarkable iron-rich rapidly expanding SNR G350.1-0.3 (Borkowski et al., 2020) is at most 600 years old (the expansion age of the fastest-moving ejecta and an upper limit to the true age, since deceleration has certainly occurred). For an age of 600 years and a distance of 4.5 kpc, again scaling to Cas A predicts a flux of 0.027 of that of Cas A for the 68 keV line. Figure 13 shows a simulation assuming (as is not the case in Cas A!) that the titanium distribution follows that of shocked iron. The strong Fe

Kα emission from G350.1-0.3 is redshifted by up to 2,600 km s^{-1}, which if true of titanium as well, would allow both the 68 and 78 keV lines to be observed, which was not the case for Cas A, potentially doubling the relative sensitivity. The required exposure times for HEX-P detections of these targets at such flux levels are too long for the proposed primary observation program, but are certainly within reach for the extended mission. We mention them here as a reminder that HEX-P can bring this unique capability to the study of supernovae.

5.2 r-process nucleosynthesis in binary NS-NS mergers

The creation of cosmic isotopes heavier than the iron group is primarily attributed to the so-called r-process, which involves rapid neutron captures compared to β-decay lifetimes (Burbidge et al., 1957; Cameron, 1957). However, it remains unclear where this nucleosynthesis occurs, as it requires neutron-rich environments with low electron fraction Y_e. Recent observations of thermal kilonova emission from ejecta produced in binary neutron-star mergers (NSMs) in gravitational wave events like GW170817 (Abbott et al., 2017) or in short gamma-ray bursts (e.g., GRB 130603B; Tanvir et al., 2013) strongly suggest a significant r-process component. In fact, these observations have established NSMs as a promising r-process site, possibly even more important than the standard case involving core-collapse supernovae (SNe) (Lattimer and Schramm, 1974). While MeV gamma-rays from r-process nuclei should provide direct evidence for NSMs, their fluxes immediately following binary NSM events are estimated to be very low ($\sim 10^{-8}$ photons s^{-1} cm^{-2} keV^{-1}) even at a close distance of 3 Mpc (Hotokezaka et al., 2016). This is below the sensitivity of current and near-future MeV gamma-ray missions. An alternative and more promising approach to explore the r-process site is to search for gamma-rays from long-lived r-process nuclei in Galactic NSMs (Wu et al., 2019; Korobkin et al.,
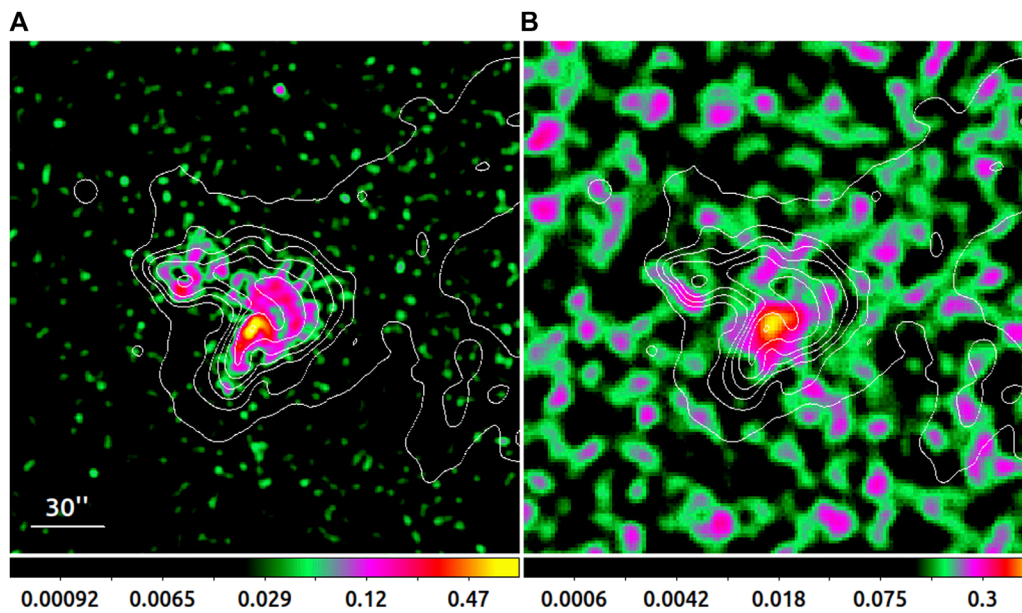
FIGURE 13
(A) Chandra Fe Kα image of G350.1−0.1 measured in the 6.3−6.8 keV band (270 ks exposure). Color bar units are counts. The white contours show the Chandra continuum image. **(B)** Simulated HEX-P image of ^{44}Ti emission from G350.1−0.1 (67−69 keV) for 2 Ms exposure. For this simulation, the Chandra Fe Kα map **(A)** was used as the input image.

2020; Wang et al., 2020; Terada et al., 2022). The radiation from r-process nuclei appears mainly in the sub-MeV band, but in older remnants, it can extend down to the hard X-ray band. The hard X-ray signals from the decay of r-process isotopes can be detected by HEX-P, making it a unique probe to study the r-process from Galactic NSMs and establishing synergy with gravitational wave observations in the multi-messenger era.

In order to assess the feasibility of detecting gamma-rays from Galactic NSMs with HEX-P, we compared the gamma-ray spectra from Galactic NSMs, at ages of τ of 100, 10^4, and 10^6 years old and located at 10 kpc, with the sensitivities of hard X-ray to gamma-ray telescopes including HEX-P (Figure 14). Since most Galactic NSMs are expected to be ~8 kpc away (Wu et al., 2019), HEX-P can detect younger NSM remnants with τ less than a few hundred years. Additionally, HEX-P may be able to detect nuclear gamma-ray lines from middle-aged NSM remnants (τ less than about a few $\times 10^3$ years), since the Doppler broadening caused by the fast motion of ejecta is much less significant than in younger remnants. Figure 14 shows that the nuclear lines from ^{229}Th (11.3 keV), ^{126}Sn (23.4 keV), ^{241}Am (26.8 keV, 59.6 keV), ^{225}Ra (40.3 keV), and ^{243}Am (43.9 keV) from Galactic NSMs with 10^4 years old are above the sensitivity of HEX-P.

Since HEX-P is not a survey-type mission, it is important to select optimal NSM candidates in advance. This can be done through a pilot survey utilizing the current hard X-ray and gamma-ray missions, such as *INTEGRAL*, *Swift*, *MAXI*, etc., or by discovering NSMs serendipitously, for instance in the HEX-P's Galactic Center
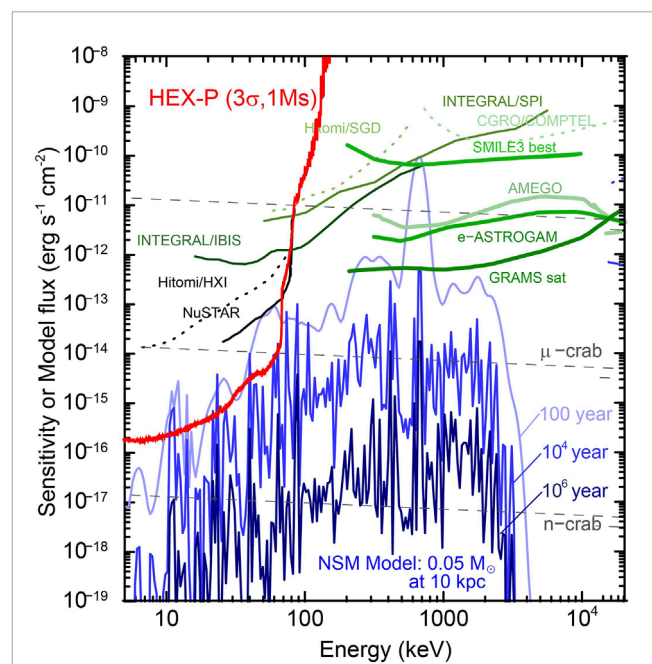

FIGURE 14
Gamma-ray spectra from NSM remnants estimated by Terada et al. (2022) at a distance of 10 kpc and with ages of 100, 10^4, and 10^6 years since the merging are shown in cyan, blue, and dark blue lines, respectively. The 3-σ sensitivities of the hard X-ray to gamma-ray missions are shown as the labeled lines. The 3-σ sensitivity of HEX-P with 1 Ms exposure is shown in red. For others, please see Figure 14 in Terada et al. (2022).
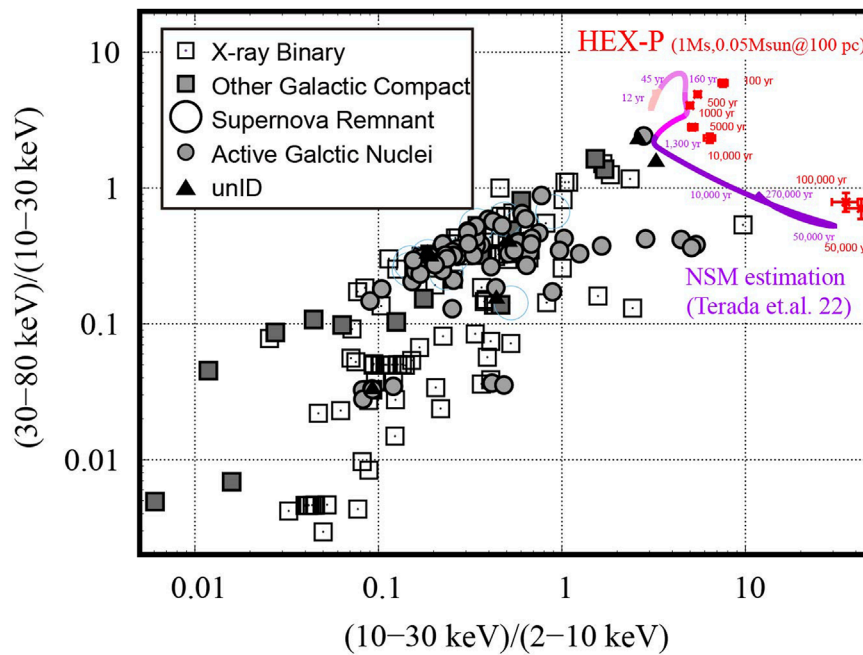
FIGURE 15
A color−color diagram of the flux ratio between the 30−80 and 10−30 keV bands versus that between the 10−30 and 2−10 keV bands. Our estimation, following the same procedure as Figure 8 in Terada et al. (2022), is shown in the purple line, and those of the X-ray objects listed in the *INTEGRAL* catalog (version 0043) are plotted in gray. The red crosses represent the expectation with 3σ errors for the NSMs at 100 pc using HEX-P with 1 Ms exposure.

survey (Mori et al., submitted to FrASS). One of the effective ways based on a pilot survey with the current gamma-ray instruments is to diagnose the spectral shape of NSMs using the color-color diagram shown in Figure 8 in Terada et al. (2022). Figure 15 displays the same diagram, but recalculated for HEX-P's energy band from 2 to 80 keV, using the simulation code adopted from Terada et al. (2022). Our simulations demonstrate that very young NSMs ($\tau < 10^3$ y) and old NSMs ($\tau > 10^4$ y) can be distinguished from other types of hard X-ray sources such as SNRs, AGNs, and XRBs. The figure also demonstrates the numerical results for the case of a nearby NSM (within 100 pc) observed by HEX-P with long exposure times (shown in red crosses in Figure 15).

Once an NSM remnant is identified by the color-color diagram analysis, a handful of nuclear lines from r-process nuclei may be detected with deeper observations of HEX-P, as already shown in Figure 14. Nuclear lines in the hard X-ray band originate mostly from nuclei in the relatively low Y_e environment, compared with those in the MeV band. Note that the hard X-ray nuclear lines are unique signatures of NSMs, while MeV gamma-ray lines could be emitted from SNe. Therefore, the hard X-ray lines potentially detectable with HEX-P, namely, ^{229}Th, ^{126}Sn, ^{241}Am, ^{225}Ra, and ^{243}Am, will provide strong evidence of r-process nucleosynthesis in NSM remnants. Among them, it is anticipated that the nuclear lines from ^{241}Am, ^{243}Am, and ^{126}Sn have constant luminosities for $\tau \sim 10^2$–10^5 years (Figure 9 in Terada et al. (2022)), yielding a few hundred photon counts with 1 Msec exposure, and therefore, making them suitable as a standard candle for estimating the source distance. Overall, searching for r-process nucleosynthesis sites in

our Galaxy is a unique scientific objective of HEX-P in the 2030s that, while somewhat risky, has the potential for significant scientific gains.

6 Conclusion

The physical processes involved in the acceleration of particles at strong shocks are particularly well exhibited in shell SNRs, for nonrelativistic shocks, and in PWNe, for relativistic shocks. These processes ought to operate across the Universe, in many environments where sources are too compact to be spatially resolved. Galactic SNRs and PWNe, closely examined by HEX-P, can serve as laboratories in which to investigate details of these processes. Major breakthroughs in understanding occurred with hard X-ray observations of the famous shell SNR SN 1006, and of the even more famous Crab Nebula. A great deal more can be learned about objects in each class with the new capabilities promised by HEX-P. The simulations described above demonstrate the kinds of advances possible in the study of particular SNRs and PWNe, and of Galactic particle acceleration in general (see Mori et al., 2021 for other types of particle accelerators). The additional, unique capability of HEX-P to study nuclear-decay line emission will improve our knowledge of the ^{44}Ti distribution in Cas A, and may detect lines from other young SNRs or in the unlikely but exciting possibility of a sufficiently nearby neutron-star binary merger event. HEX-P clearly stands out as the foremost X-ray observatory for cosmic accelerators and nuclear astrophysics in the 2030s.

Data availability statement

The original contributions presented in the study are included in the article. Further inquiries may be directed to the corresponding author.

Author contributions

SR: Writing–original draft. HA: Writing–original draft. MA: Writing–original draft. JA: Writing–original draft. CF: Writing–original draft. KM: Writing–original draft. MN: Writing–original draft. JP: Writing–original draft. YT: Writing–original draft. JW: Writing–original draft. AB: Writing–review and editing. PB: Writing–review and editing. RD: Writing–review and editing. JE: Writing–review and editing. SG: Writing–review and editing. JoG: Writing–review and editing. BG: Writing–review and editing. JaG: Project administration, Writing–review and editing. CK: Writing–review and editing. SK: Writing–review and editing. BI: Writing–review and editing. KM: Project administration, Writing–review and editing. SM: Writing–review and editing. YM: Writing–review and editing. HO: Writing–review and editing. BO: Writing–review and editing. TS: Writing–review and editing. R-YS: Writing–review and editing. DS: Project administration, Writing–review and editing. NT: Writing–review and editing. GY: Writing–review and editing. AZ: Writing–review and editing.

Funding

Acknowledgments

Conflict of interest

The authors declare that the research was conducted in the absence of any commercial or financial relationships that could be construed as a potential conflict of interest.

Publisher's note

All claims expressed in this article are solely those of the authors and do not necessarily represent those of their affiliated organizations, or those of the publisher, the editors and the reviewers. Any product that may be evaluated in this article, or claim that may be made by its manufacturer, is not guaranteed or endorsed by the publisher.

References

Abbott, B. P., Abbott, R., Abbott, T. D., Acernese, F., Ackley, K., Adams, C., et al. (2017). GW170817: observation of gravitational waves from a binary neutron star inspiral. *PhRvL* 119, 161101. doi:10.1103/PhysRevLett.119.161101

Abdelmaguid, M., Gelfand, J. D., Gotthelf, E., and Straal, S. (2023). Broadband X-ray spectroscopy of the pulsar wind nebula in HESS j1640-465. *ApJ* 946, 40. doi:10.3847/1538-4357/acbd30

Abeysekara, A. U., Albert, A., Alfaro, R., Alvarez, C., Álvarez, J. D., Arceo, R., et al. (2017a). Extended gamma-ray sources around pulsars constrain the origin of the positron flux at Earth. *Science* 358, 911–914. doi:10.1126/science.aan4880

Acciari, V. A., Aliu, E., Arlen, T., Aune, T., Beilicke, M., Benbow, W., et al. (2011). Discovery of TeV gamma-ray emission from Tycho's supernova remnant. *ApJL* 730, L20. doi:10.1088/2041-8205/730/2/L20

Adams, C. B., Benbow, W., Brill, A., Brose, R., Buchovecky, M., Capasso, M., et al. (2021). VERITAS observations of the galactic center region at multi-TeV gamma-ray energies. *ApJ* 913, 115. doi:10.3847/1538-4357/abf926

Aguilar, M., Ali Cavasonza, L., Alpat, B., Ambrosi, G., Arruda, L., Attig, N., et al. (2019). Towards understanding the origin of cosmic-ray electrons. *PhRvL* 122, 101101. doi:10.1103/PhysRevLett.122.101101

Aharonian, F., Akhperjanian, A. G., Aye, K.-M., Bazer-Bachi, A. R., Beilicke, M., Benbow, W., et al. (2005). Very high energy gamma rays from the composite SNR G 0.9+0.1. *A&A* 432, L25–L29. doi:10.1051/0004-6361:200500022

Alp, D., Larsson, J., and Fransson, C. (2021). Thermal emission and radioactive lines, but No pulsar, in the broadband X-ray spectrum of supernova 1987A. *ApJ* 916, 76. doi:10.3847/1538-4357/ac052d

Alp, D., Larsson, J., Fransson, C., Indebetouw, R., Jerkstrand, A., Ahola, A., et al. (2018). The 30 Year search for the compact object in SN 1987A. *ApJ* 864, 174. doi:10.3847/1538-4357/aad739

An, H. (2019). NuSTAR hard X-ray studies of the pulsar wind nebula 3C 58. *ApJ* 876, 150. doi:10.3847/1538-4357/ab18a6

An, H., Madsen, K. K., Reynolds, S. P., Kaspi, V. M., Harrison, F. A., Boggs, S. E., et al. (2014). High-energy X-ray imaging of the pulsar wind nebula MSH 15-52: constraints on particle acceleration and transport. *ApJ* 793, 90. doi:10.1088/0004-637X/793/2/90

Arnaud, K. A. (1996). "XSPEC: the first ten years," in *Astronomical data analysis software and systems V*. Editors G. H. Jacoby, and J. Barnes (USA: IEEE), 17.

Atoyan, A., and Dermer, C. D. (2012). Gamma rays from the Tycho supernova remnant: multi-zone versus single-zone modeling. *ApJL* 749, L26. doi:10.1088/2041-8205/749/2/L26

Bamba, A., Anada, T., Dotani, T., Mori, K., Yamazaki, R., Ebisawa, K., et al. (2010). X-Ray evolution of pulsar wind nebulae. *ApJL* 719, L116–L120. doi:10.1088/2041-8205/719/2/L116

Bamba, A., Shibata, S., Tanaka, S. J., Mori, K., Uchida, H., Terada, Y., et al. (2022). Spectral break of energetic pulsar wind nebulae detected with wideband X-ray observations. *PASJ* 74, 1186–1197. doi:10.1093/pasj/psac062

Bamba, A., Yamazaki, R., Yoshida, T., Terasawa, T., and Koyama, K. (2005). A spatial and spectral study of nonthermal filaments in historical supernova remnants: observational results with Chandra. *ApJ* 621, 793–802. doi:10.1086/427620

Bandiera, R. (2008). On the X-ray feature associated with the Guitar nebula. *A&A* 490, L3–L6. doi:10.1051/0004-6361:200810666

Bandiera, R., Bucciantini, N., Martín, J., Olmi, B., and Torres, D. F. (2020). Reverberation of pulsar wind nebulae (I): impact of the medium properties and other parameters upon the extent of the compression. *MNRAS* 499, 2051–2062. doi:10.1093/mnras/staa2956

Bandiera, R., Bucciantini, N., Martín, J., Olmi, B., and Torres, D. F. (2023). Reverberation of pulsar wind nebulae - II. Anatomy of the 'thin-shell' evolution. *MNRAS* 520, 2451–2472. doi:10.1093/mnras/stad134

Berezhko, E. G., Ksenofontov, L. T., and Völk, H. J. (2013). The nature of gamma-ray emission of Tycho's supernova remnant. *ApJ* 763, 14. doi:10.1088/0004-637X/763/1/14

Bleeker, J. A. M., Willingale, R., van der Heyden, K., Dennerl, K., Kaastra, J. S., Aschenbach, B., et al. (2001). Cassiopeia A: on the origin of the hard X-ray continuum and the implication of the observed O VIII Ly-α/Ly-β distribution. *A&A* 365, L225–L230. doi:10.1051/0004-6361:20000048

Borkowski, K. J., Miltich, W., and Reynolds, S. P. (2020). Expansion and age of the supernova remnant g350.1-0.3: high-velocity iron ejecta from a core-collapse event. *ApJL* 905, L19. doi:10.3847/2041-8213/abcda7

Borkowski, K. J., Reynolds, S. P., Green, D. A., Hwang, U., Petre, R., Krishnamurthy, K., et al. (2010). Radioactive scandium in the youngest galactic supernova remnant G1.9+0.3. *ApJL* 724, L161–L165. –L165. doi:10.1088/2041-8205/724/2/L161

Bucciantini, N., Blondin, J. M., Del Zanna, L., and Amato, E. (2003). Spherically symmetric relativistic MHD simulations of pulsar wind nebulae in supernova remnants. *A&A* 405, 617–626. doi:10.1051/0004-6361:20030624

Burbidge, E. M., Burbidge, G. R., Fowler, W. A., and Hoyle, F. (1957). Synthesis of the elements in stars. *Rev. Mod. Phys.* 29, 547–650. doi:10.1103/RevModPhys.29.547

Burgess, D. A., Mori, K., Gelfand, J. D., Hailey, C. J., Tokayer, Y. M., Woo, J., et al. (2022). The eel pulsar wind nebula: a PeVatron-candidate origin for hawc j1826-128 and hess j1826-130. *ApJ* 930, 148. doi:10.3847/1538-4357/ac650a

Cameron, A. G. W. (1957). Nuclear reactions in stars and nucleogenesis. *PASP* 69, 201. doi:10.1086/127051

Camilo, F., Ransom, S. M., Gaensler, B. M., and Lorimer, D. R. (2009). Discovery of the energetic pulsar j1747-2809 in the supernova remnant G0.9+0.1. *ApJL* 700, L34–L38. –L38. doi:10.1088/0004-637X/700/1/L34

Cao, Z., Aharonian, F., An, Q., Axikegu, Bai, Y. X., Bao, Y. W., et al. (2023). *The first LHAASO catalog of gamma-ray sources*, arXiv:2305.1703010.48550/arXiv

Cao, Z., Aharonian, F. A., An, Q., Axikegu, Bai, L. X., Bai, Y. X., et al. (2021). Ultrahigh-energy photons up to 1.4 petaelectronvolts from 12 γ-ray Galactic sources. *Nature* 594, 33–36. doi:10.1038/s41586-021-03498-z

Carlton, A. K., Borkowski, K. J., Reynolds, S. P., Hwang, U., Petre, R., Green, D. A., et al. (2011). Expansion of the youngest galactic supernova remnant G1.9+0.3. *ApJL* 737, L22. doi:10.1088/2041-8205/737/1/L22

Cherenkov Telescope Array Consortium, T. (2023). *Sensitivity of the Cherenkov telescope Array to TeV photon emission from the large magellanic cloud*. arXiv:2305.1670710.48550/arXiv.

Chevalier, R. A., Kirshner, R. P., and Raymond, J. C. (1980). The optical emission from a fast shock wave with application to supernova remnants. *ApJ* 235, 186–195. doi:10.1086/157623

Cholis, I., and Hooper, D. (2013). Dark matter and pulsar origins of the rising cosmic ray positron fraction in light of new data from the AMS. *PhRvD* 88, 023013. doi:10.1103/PhysRevD.88.023013

Cigan, P., Matsuura, M., Gomez, H. L., Indebetouw, R., Abellán, F., Gabler, M., et al. (2019). High angular resolution ALMA images of dust and molecules in the SN 1987A ejecta. *ApJ* 886, 51. doi:10.3847/1538-4357/ab4b46

Dauser, T., Falkner, S., Lorenz, M., Kirsch, C., Peille, P., Cucchetti, E., et al. (2019). SIXTE: a generic X-ray instrument simulation toolkit. *A&A* 630, A66. doi:10.1051/0004-6361/201935978

Della Torre, S., Gervasi, M., Rancoita, P. G., Rozza, D., and Treves, A. (2015). Pulsar Wind Nebulae as a source of the observed electron and positron excess at high energy: the case of Vela-X. *J. High Energy Astrophysics* 8, 27–34. doi:10.1016/j.jheap.2015.08.001

Del Zanna, L., Amato, E., and Bucciantini, N. (2004). Axially symmetric relativistic MHD simulations of Pulsar Wind Nebulae in Supernova Remnants. On the origin of torus and jet-like features. *A&A* 421, 1063–1073. doi:10.1051/0004-6361:20035936

de Oña Wilhelmi, E., López-Coto, R., Amato, E., and Aharonian, F. (2022). On the potential of bright, young pulsars to power ultrahigh gamma-ray sources. *ApJL* 930, L2. doi:10.3847/2041-8213/ac66cf

Diesing, R., and Caprioli, D. (2021). Steep cosmic-ray spectra with revised diffusive shock acceleration. *ApJ* 922, 1. doi:10.3847/1538-4357/ac22fe

Eraerds, T., Antonelli, V., Davis, C., Hall, D., Hetherington, O., Holland, A., et al. (2021). Enhanced simulations on the athena/wide field imager instrumental background. *J. Astronomical Telesc. Instrum. Syst.* 7, 034001. doi:10.1117/1.JATIS.7.3.034001

Eriksen, K. A., Hughes, J. P., Badenes, C., Fesen, R., Ghavamian, P., Moffett, D., et al. (2011). Evidence for particle acceleration to the knee of the cosmic ray spectrum in Tycho's supernova remnant. *ApJL* 728, L28. doi:10.1088/2041-8205/728/2/L28

Fiori, M., Zampieri, L., Burtovoi, A., Caraveo, P., and Tibaldo, L. (2020). Constraining models of the pulsar wind nebula in SNR G0.9+0.1 via simulation of its detection properties using the Cherenkov Telescope Array. *MNRAS* 499, 3494–3509. doi:10.1093/mnras/staa3039

Frank, K. A., Zhekov, S. A., Park, S., McCray, R., Dwek, E., and Burrows, D. N. (2016). Chandra observes the end of an era in SN 1987A. *ApJ* 829, 40. doi:10.3847/0004-637X/829/1/40

Fraschetti, F., Katsuda, S., Sato, T., Jokipii, J. R., and Giacalone, J. (2018). Vortical amplification of the magnetic field at an inward shock of supernova remnant cassiopeia a. *Phys. Rev. Lett.* 120, 251101. doi:10.1103/PhysRevLett.120.251101

Fryer, C. L., Burns, E., Hungerford, A., Safi-Harb, S., Wollaeger, R. T., Miller, R. S., et al. (2023). Multi-messenger diagnostics of the engine behind core-collapse supernovae. *arXiv e-prints* , arXiv:2305.0613410.48550/arXiv.2305.06134

Gaensler, B. M., Pivovaroff, M. J., and Garmire, G. P. (2001). [ITAL]Chandra[/ITAL] observations of the pulsar wind nebula in supernova remnant G0.9+0.1. *ApJL* 556, L107–L111. –L111. doi:10.1086/322982

Gelfand, J. D., Slane, P. O., and Zhang, W. (2009). A dynamical model for the evolution of a pulsar wind nebula inside a nonradiative supernova remnant. *ApJ* 703, 2051–2067. –2067. doi:10.1088/0004-637X/703/2/2051

Giordano, F., Naumann-Godo, M., Ballet, J., Bechtol, K., Funk, S., Lande, J., et al. (2012). Fermi large area telescope detection of the young supernova remnant Tycho. *ApJL* 744, L2. doi:10.1088/2041-8205/744/1/L2

Gotthelf, E. V., Safi-Harb, S., Straal, S. M., and Gelfand, J. D. (2021). X-ray spectroscopy of the highly magnetized pulsar PSR j1846-0258, its wind nebula, and hosting supernova remnant kes 75. *ApJ* 908, 212. doi:10.3847/1538-4357/abd32b

Greco, E., Miceli, M., Orlando, S., Olmi, B., Bocchino, F., Nagataki, S., et al. (2021). Indication of a pulsar wind nebula in the hard X-ray emission from SN 1987A. *ApJL* 908, L45. doi:10.3847/2041-8213/abdf5a

Greco, E., Miceli, M., Orlando, S., Olmi, B., Bocchino, F., Nagataki, S., et al. (2022). Additional evidence for a pulsar wind nebula in the heart of SN 1987A from multiepoch X-ray data and MHD modeling. *ApJ* 931, 132. doi:10.3847/1538-4357/ac679d

Grefenstette, B. W., Fryer, C. L., Harrison, F. A., Boggs, S. E., DeLaney, T., Laming, J. M., et al. (2017). The distribution of radioactive ^{44}Ti in cassiopeia A. *ApJ* 834, 19. doi:10.3847/1538-4357/834/1/19

Grefenstette, B. W., Harrison, F. A., Boggs, S. E., Reynolds, S. P., Fryer, C. L., Madsen, K. K., et al. (2014). Asymmetries in core-collapse supernovae from maps of radioactive ^{44}Ti in CassiopeiaA. *Nature* 506, 339–342. doi:10.1038/nature12997

Grefenstette, B. W., Reynolds, S. P., Harrison, F. A., Humensky, T. B., Boggs, S. E., Fryer, C. L., et al. (2015). Locating the most energetic electrons in cassiopeia A. *ApJ* 802, 15. doi:10.1088/0004-637X/802/1/15

Guest, B. T., Safi-Harb, S., and Tang, X. (2019). The deepest Chandra X-ray study of the plerionic supernova remnant G21.5-0.9. *MNRAS* 482, 1031–1042. doi:10.1093/mnras/sty2635

Halpern, J. P., Tomsick, J. A., Gotthelf, E. V., Camilo, F., Ng, C. Y., Bodaghee, A., et al. (2014). Discovery of X-ray pulsations from the INTEGRAL source IGR j11014-6103. *ApJL* 795, L27. doi:10.1088/2041-8205/795/2/L27

Hanbury Brown, R., and Hazard, C. (1952). Radio-frequency radiation from Tycho brahe's supernova (A.D. 1572). *Nature* 170, 364–365. doi:10.1038/170364a0

Harrison, F. A., Craig, W. W., Christensen, F. E., Hailey, C. J., Zhang, W. W., Boggs, S. E., et al. (2013). The nuclear spectroscopic telescope Array (NuSTAR) high-energy X-ray mission. *ApJ* 770, 103. doi:10.1088/0004-637X/770/2/103

Hattori, S., Straal, S. M., Zhang, E., Temim, T., Gelfand, J. D., and Slane, P. O. (2020). The nonstandard properties of a "standard" PWN: unveiling the mysteries of PWN g21.5-0.9 using its IR and X-ray emission. *ApJ* 904, 32. doi:10.3847/1538-4357/abba32

Helder, E. A., and Vink, J. (2008). Characterizing the nonthermal emission of cassiopeia A. *ApJ* 686, 1094–1102. doi:10.1086/591242

H.E.S.S. Collaboration, Abdalla, H., Abramowski, A., Aharonian, F., Ait Benkhali, F., Akhperjanian, A. G., Andersson, T., et al. (2018). The population of TeV pulsar wind nebulae in the H.E.S.S. Galactic Plane Survey. *A&A* 612, A2. doi:10.1051/0004-6361/201629377

H.E.S.S. Collaboration, Aharonian, F., Ait Benkhali, F., Aschersleben, J., Ashkar, H., Backes, M., Barbosa Martins, V., et al. (2023). Detection of extended γ-ray emission around the Geminga pulsar with H.E.S.S *A&A* 673, A148. doi:10.1051/0004-6361/202245776

Helfand, D. J., and Becker, R. H. (1987). G0.9+0.1 and the emerging class of composite supernova remnants. *ApJ* 314, 203. doi:10.1086/165050

Hitomi Collaboration, Aharonian, F., Akamatsu, H., Akimoto, F., Allen, S. W., Angelini, L., Audard, M., et al. (2018). Hitomi X-ray observation of the pulsar wind nebula g21.5-0.9. *PASJ* 70, 38. doi:10.1093/pasj/psy027

Holler, M., Schöck, F. M., Eger, P., Kießling, D., Valerius, K., and Stegmann, C. (2012). Spatially resolved X-ray spectroscopy and modeling of the nonthermal emission of the pulsar wind nebula in G0.9+0.1. *A&A* 539, A24. doi:10.1051/0004-6361/201118121

Hotokezaka, K., Wanajo, S., Tanaka, M., Bamba, A., Terada, Y., and Piran, T. (2016). Radioactive decay products in neutron star merger ejecta: heating efficiency and γ-ray emission. *MNRAS* 459, 35–43. doi:10.1093/mnras/stw404

Hwang, U., Decourchelle, A., Holt, S. S., and Petre, R. (2002). Thermal and nonthermal X-ray emission from the forward shock in Tycho's supernova remnant. *ApJ* 581, 1101–1115. doi:10.1086/344366

Jansen, F., Lumb, D., Altieri, B., Clavel, J., Ehle, M., Erd, C., et al. (2001). XMM-Newton observatory. I. The spacecraft and operations. *A&A* 365, L1–L6. doi:10.1051/0004-6361:20000036

Kargaltsev, O., Pavlov, G. G., Klingler, N., and Rangelov, B. (2017). Pulsar wind nebulae created by fast-moving pulsars. *J. Plasma Phys.* 83, 635830501. doi:10.1017/S0022377817000630

Kennel, C. F., and Coroniti, F. V. (1984a). Confinement of the Crab pulsar's wind by its supernova remnant. *ApJ* 283, 694–709. doi:10.1086/162356

Kennel, C. F., and Coroniti, F. V. (1984b). Magnetohydrodynamic model of Crab nebula radiation. *ApJ* 283, 710–730. doi:10.1086/162357

Klingler, N., Hare, J., Kargaltsev, O., Pavlov, G. G., and Tomsick, J. (2022). *A NuSTAR and Chandra investigation of the misaligned outflow of PSR j1101-6101 and the Lighthouse pulsar wind nebula.* arXiv:2212.0395210.48550/arXiv.2212.03952.

Kolb, C., Blondin, J., Slane, P., and Temim, T. (2017). Evolution of a pulsar wind nebula within a composite supernova remnant. *ApJ* 844, 1. doi:10.3847/1538-4357/aa75ce

Komissarov, S. S., and Lyubarsky, Y. E. (2004). Synchrotron nebulae created by anisotropic magnetized pulsar winds. *MNRAS* 349, 779–792. doi:10.1111/j.1365-2966.2004.07597.x

Korobkin, O., Hungerford, A. M., Fryer, C. L., Mumpower, M. R., Misch, G. W., Sprouse, T. M., et al. (2020). Gamma rays from kilonova: a potential probe of r-process nucleosynthesis. *ApJ* 889, 168. doi:10.3847/1538-4357/ab64d8

Krause, O., Birkmann, S. M., Usuda, T., Hattori, T., Goto, M., Rieke, G. H., et al. (2008a). The cassiopeia A supernova was of type IIb. *Science* 320, 1195–1197. doi:10.1126/science.1155788

Krause, O., Tanaka, M., Usuda, T., Hattori, T., Goto, M., Birkmann, S., et al. (2008b). Tycho Brahe's 1572 supernova as a standard typeIa as revealed by its light-echo spectrum. *Nature* 456, 617–619. doi:10.1038/nature07608

Lattimer, J. M., and Schramm, D. N. (1974). Black-hole-neutron-star collisions. *ApJL* 192, L145. doi:10.1086/181612

Lopez, L. A., Grefenstette, B. W., Reynolds, S. P., An, H., Boggs, S. E., Christensen, F. E., et al. (2015). A spatially resolved study of the synchrotron emission and titanium in Tycho's supernova remnant using NuSTAR. *ApJ* 814, 132. doi:10.1088/0004-637X/814/2/132

Madsen, K. K., García, J. A., Stern, D., Armini, R., Basso, S., Coutinho, D., et al. (2023). The High Energy X-ray Probe (HEX-P): instrument and mission profile. arXiv:2312.04678.

Madsen, K. K., Beardmore, A. P., Forster, K., Guainazzi, M., Marshall, H. L., Miller, E. D., et al. (2017a). IACHEC cross-calibration of Chandra, NuSTAR, Swift, suzaku, XMM-Newton with 3C 273 and PKS 2155-304. *AJ* 153, 2. doi:10.3847/1538-3881/153/1/2

Madsen, K. K., Christensen, F. E., Craig, W. W., Forster, K. W., Grefenstette, B. W., Harrison, F. A., et al. (2017b). *Observational artifacts of NuSTAR: ghost rays and stray light.* arXiv:1711.0271910.48550/arXiv. 1711.02719.

Madsen, K. K., Fryer, C. L., Grefenstette, B. W., Lopez, L. A., Reynolds, S., and Zoglauer, A. (2020). NuSTAR observations of g11.2-0.3. *ApJ* 889, 23. doi:10.3847/1538-4357/ab54ca

Madsen, K. K., Reynolds, S., Harrison, F., An, H., Boggs, S., Christensen, F. E., et al. (2015a). Broadband X-ray imaging and spectroscopy of the Crab nebula and pulsar with NuSTAR. *ApJ* 801, 66. doi:10.1088/0004-637X/801/1/66

Maeda, K., Röpke, F. K., Fink, M., Hillebrandt, W., Travaglio, C., and Thielemann, F. K. (2010). Nucleosynthesis in two-dimensional delayed detonation models of type Ia supernova explosions. *ApJ* 712, 624–638. doi:10.1088/0004-637X/712/1/624

Maeda, Y., Uchiyama, Y., Bamba, A., Kosugi, H., Tsunemi, H., Helder, E. A., et al. (2009). Suzaku X-ray imaging and spectroscopy of cassiopeia A. *PASJ* 61, 1217–1228. doi:10.1093/pasj/61.6.1217

Magkotsios, G., Timmes, F. X., Hungerford, A. L., Fryer, C. L., Young, P. A., and Wiescher, M. (2010). Trends in ^{44}Ti and ^{56}Ni from core-collapse supernovae. *ApJS* 191, 66–95. doi:10.1088/0067-0049/191/1/66

Manconi, S., Di Mauro, M., and Donato, F. (2020). Contribution of pulsars to cosmic-ray positrons in light of recent observation of inverse-Compton halos. *PhRvD* 102, 023015. doi:10.1103/PhysRevD.102.023015

Mori, K., An, H., Burgess, D., Capasso, M., Dingus, B., Gelfand, J., et al. (2021). *NuSTAR broad-band X-ray observational campaign of energetic pulsar wind nebulae in synergy with VERITAS, HAWC and Fermi gamma-ray telescopes.* arXiv:2108.00557.

Mori, K., Burrows, D. N., Hester, J. J., Pavlov, G. G., Shibata, S., and Tsunemi, H. (2004). Spatial variation of the X-ray spectrum of the Crab nebula. *ApJ* 609, 186–193. doi:10.1086/421011

Ng, C. Y., and Romani, R. W. (2004). Fitting pulsar wind tori. *ApJ* 601, 479–484. doi:10.1086/380486

Nynka, M., Hailey, C. J., Reynolds, S. P., An, H., Baganoff, F. K., Boggs, S. E., et al. (2014). NuSTAR study of hard X-ray morphology and spectroscopy of PWN g21.5-0.9. *ApJ* 789, 72. doi:10.1088/0004-637X/789/1/72

Okuno, T., Tanaka, T., Uchida, H., Aharonian, F. A., Uchiyama, Y., Tsuru, T. G., et al. (2020). Time variability of nonthermal X-ray stripes in Tycho's supernova remnant with Chandra. *ApJ* 894, 50. doi:10.3847/1538-4357/ab837e

Olmi, B., and Bucciantini, N. (2019). On the origin of jet-like features in bow shock pulsar wind nebulae. *MNRAS* 490, 3608–3615. doi:10.1093/mnras/stz2819

Olmi, B., and Bucciantini, N. (2023). The dawes review 11: from young to old: the evolutionary path of pulsar wind nebulae. *PASA* 40, e007. doi:10.1017/pasa.2023.5

Orlando, S., Wongwathanarat, A., Janka, H. T., Miceli, M., Nagataki, S., Ono, M., et al. (2022). Evidence for past interaction with an asymmetric circumstellar shell in the young SNR Cassiopeia A. *A&A* 666, A2. A2. doi:10.1051/0004-6361/202243258

Parizot, E., Marcowith, A., Ballet, J., and Gallant, Y. A. (2006). Observational constraints on energetic particle diffusion in young supernovae remnants: amplified magnetic field and maximum energy. *A&A* 453, 387–395. doi:10.1051/0004-6361:20064985

Park, J., Kim, C., Woo, J., An, H., Mori, K., Reynolds, S. P., et al. (2023a). A broadband X-ray study of the rabbit pulsar wind nebula powered by PSR j1418-6058. *ApJ* 945, 66. doi:10.3847/1538-4357/acba0e

Park, J., Kim, C., Woo, J., An, H., Mori, K., Reynolds, S. P., et al. (2023b). X-ray studies of the pulsar PSR j1420-6048 and its TeV pulsar wind nebula in the kookaburra region. *ApJ* 945, 33. doi:10.3847/1538-4357/acb1b0

Pavan, L., Pühlhofer, G., Bordas, P., Audard, M., Balbo, M., Bozzo, E., et al. (2016). Closer view of the IGR J11014-6103 outflows. *A&A* 591, A91. doi:10.1051/0004-6361/201527703

Porquet, D., Decourchelle, A., and Warwick, R. S. (2003). XMM-Newton spectral analysis of the Pulsar Wind Nebula within the composite SNR G0.9+0.1. *A&A* 401, 197–203. doi:10.1051/0004-6361:20021670

Porter, T. A., Jóhannesson, G., and Moskalenko, I. V. (2022). The GALPROP cosmic-ray propagation and nonthermal emissions framework: release v57. *ApJS* 262, 30. doi:10.3847/1538-4365/ac80f6

Pravdo, S. H., and Smith, B. W. (1979). X-ray evidence for electron-ion equilibrium and ionization nonequilibrium in Young supernova remnants. *ApJL* 234, L195. doi:10.1086/183138

Renaud, M., Marandon, V., Gotthelf, E. V., Rodriguez, J., Terrier, R., Mattana, F., et al. (2010). Discover of a highly eneregtic pulsar associated with igr j14003–6326 in the young uncataloged galaactic supernova remnant G310.6–1.6. *ApJ* 716, 663–670. doi:10.1088/0004-637X/716/1/663

Reynolds, S. P. (2009). Synchrotron-loss spectral breaks in pulsar-wind nebulae and extragalactic jets. *ApJ* 703, 662–670. doi:10.1088/0004-637X/703/1/662

Reynolds, S. P. (2016). Hard X-ray emission from pulsar-wind nebulae. *J. Plasma Phys.* 82, 635820501. doi:10.1017/S0022377816000751

Reynolds, S. P., Borkowski, K. J., Green, D. A., Hwang, U., Harrus, I., and Petre, R. (2008). The youngest galactic supernova remnant: G1.9+0.3. *ApJL* 680, L41–L44. doi:10.1086/589570

Reynolds, S. P., Borkowski, K. J., Green, D. A., Hwang, U., Harrus, I., and Petre, R. (2009). X-ray spectral variations in the youngest galactic supernova remnant G1.9+0.3. *ApJL* 695, L149–L153. doi:10.1088/0004-637X/695/2/L149

Reynolds, S. P., Borkowski, K. J., and Gwynne, P. H. (2018). Expansion and brightness changes in the pulsar-wind nebula in the composite supernova remnant Kes 75. *ApJ* 856, 133. doi:10.3847/1538-4357/aab3d3

Reynolds, S., An, H., Abdelmaguid, M., Alford, J., Fryer, C., Mori, K., et al. (2023). High-energy astrophysics research enabled by the probe-class mission concept HEX-P. Front. Astron. Space Sci. 10. doi:10.3389/fspas.2023.1321278

Reynolds, S. P., and Chevalier, R. A. (1984). Evolution of pulsar-driven supernova remnants. *ApJ* 278, 630–648. doi:10.1086/161831

Reynoso, E. M., Moffett, D. A., Goss, W. M., Dubner, G. M., Dickel, J. R., Reynolds, S. P., et al. (1997). A VLA study of the expansion of Tycho's supernova remnant. *ApJ* 491, 816–828. doi:10.1086/304997

Sato, T., Katsuda, S., Morii, M., Bamba, A., Hughes, J. P., Maeda, Y., et al. (2018). X-ray measurements of the particle acceleration properties at inward shocks in Cassiopeia A. *ApJ* 853, 46. doi:10.3847/1538-4357/aaa021

Sironi, L., and Spitkovsky, A. (2009). Particle acceleration in relativistic magnetized collisionless pair shocks: dependence of shock acceleration on magnetic obliquity. *ApJ* 698, 1523–1549. doi:10.1088/0004-637X/698/2/1523

Sironi, L., and Spitkovsky, A. (2014). Relativistic reconnection: an efficient source of non-thermal particles. *ApJL* 783, L21. doi:10.1088/2041-8205/783/1/L21

Sudoh, T., Linden, T., and Beacom, J. F. (2019). TeV halos are everywhere: prospects for new discoveries. *PhRvD* 100, 043016. doi:10.1103/PhysRevD.100.043016

Tanaka, S. J., and Takahara, F. (2011). Study of four young TeV pulsar wind nebulae with a spectral evolution model. *ApJ* 741, 40. doi:10.1088/0004-637X/741/1/40

Tanvir, N. R., Levan, A. J., Fruchter, A. S., Hjorth, J., Hounsell, R. A., Wiersema, K., et al. (2013). A 'kilonova' associated with the short-duration γ-ray burst GRB 130603B. *Nature* 500, 547–549. doi:10.1038/nature12505

Terada, Y., Miwa, Y., Ohsumi, H., Fujimoto, S.-i., Katsuda, S., Bamba, A., et al. (2022). Gamma-ray diagnostics of r-process nucleosynthesis in the remnants of galactic binary neutron-star mergers. *ApJ* 933, 111. doi:10.3847/1538-4357/ac721f

Torres, D. F., Cillis, A., Martín, J., and de Oña Wilhelmi, E. (2014). Time-dependent modeling of TeV-detected, young pulsar wind nebulae. *J. High Energy Astrophysics* 1, 31–62. doi:10.1016/j.jheap.2014.02.001

Uchiyama, Y., and Aharonian, F. A. (2008). Fast variability of nonthermal X-ray emission in cassiopeia A: probing electron acceleration in reverse-shocked ejecta. *ApJL* 677, L105–L108. doi:10.1086/588190

Vance, G. S., Young, P. A., Fryer, C. L., and Ellinger, C. I. (2020). Titanium and iron in the cassiopeia A supernova remnant. *ApJ* 895, 82. doi:10.3847/1538-4357/ab8ade

Van Etten, A., and Romani, R. W. (2011). Multi-zone modeling of the pulsar wind nebula hess j 1825–137. *Astrophysical J.* 742, 62. doi:10.1088/0004-637x/742/2/62

Vink, J. (2012). Supernova remnants: the X-ray perspective. *AAPR* 20, 49. doi:10.1007/s00159-011-0049-1

Vink, J., Kaastra, J. S., Bleeker, J. A. M., and Bloemen, H. (2000). The hard X-ray emission and 44ti emission of Cas A. *Adv. Space Res.* 25, 689–694. doi:10.1016/S0273-1177(99)00823-6

Vink, J., Prokhorov, D., Ferrazzoli, R., Slane, P., Zhou, P., Asakura, K., et al. (2022). X-ray polarization detection of cassiopeia A with IXPE. *ApJ* 938, 40. doi:10.3847/1538-4357/ac8b7b

Wang, X., N3AS Collaboration, Vassh, N., FIRE collaboration, Sprouse, T., Mumpower, M., Vogt, R., Randrup, J., et al. (2020). MeV gamma rays from fission: a distinct signature of actinide production in neutron star mergers. *ApJL* 903, L3. doi:10.3847/2041-8213/abbe18

Warren, J. S., Hughes, J. P., Badenes, C., Ghavamian, P., McKee, C. F., Moffett, D., et al. (2005). Cosmic-ray acceleration at the forward shock in Tycho's supernova remnant: evidence from Chandra X-ray observations. *ApJ* 634, 376–389. doi:10.1086/496941

Wik, D. R., Hornstrup, A., Molendi, S., Madejski, G., Harrison, F. A., Zoglauer, A., et al. (2014). NuSTAR observations of the bullet cluster: constraints on inverse compton emission. *ApJ* 792, 48. doi:10.1088/0004-637X/792/1/48

Wongwathanarat, A., Janka, H.-T., Müller, E., Pllumbi, E., and Wanajo, S. (2017). Production and distribution of ^{44}Ti and ^{56}Ni in a three-dimensional supernova model resembling cassiopeia A. *ApJ* 842, 13. doi:10.3847/1538-4357/aa72de

Woo, J., An, H., Gelfand, J. D., Hailey, C. J., Mori, K., Mukherjee, R., et al. (2023). *Hard X-ray observation and multiwavelength study of the PeVatron candidate pulsar wind nebula "Dragonfly"*. arXiv:2306.0734710. 48550/arXiv.2306.07347.

Wu, M.-R., Banerjee, P., Metzger, B. D., Martínez-Pinedo, G., Aramaki, T., Burns, E., et al. (2019). Finding the remnants of the Milky way's last neutron star mergers. *ApJ* 880, 23. doi:10.3847/1538-4357/ab2593

Xi, S.-Q., Liu, R.-Y., Huang, Z.-Q., Fang, K., and Wang, X.-Y. (2019). GeV observations of the extended pulsar wind nebulae constrain the pulsar interpretations of the cosmic-ray positron excess. *ApJ* 878, 104. doi:10.3847/1538-4357/ab20c9

Yüksel, H., Kistler, M. D., and Stanev, T. (2009). TeV gamma rays from geminga and the origin of the GeV positron excess. *PhRvL* 103, 051101. doi:10.1103/PhysRevLett.103.051101

Zoglauer, A., Reynolds, S. P., An, H., Boggs, S. E., Christensen, F. E., Craig, W. W., et al. (2015). The hard X-ray view of the young supernova remnant G1.9+0.3. *ApJ* 798, 98. doi:10.1088/0004-637X/798/2/98